

https://dspace.org/

The thermal response of brake disc at varying speeds

Zedi, Shaun

2018

https://hdl.handle.net/10539/27709

Zedi, Shaun (2018) The thermal response of brake discs at varying speeds, University of the Witwatersrand, Johannesburg, https://hdl.handle.net/10539/27709

Downloaded from a DSpace repository. https://dspace.org/

THE THERMAL RESPONSE OF BRAKE DISCS AT VARYING SPEEDS

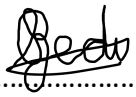
Shaun Zedi

A dissertation submitted to the Faculty of Engineering and the Built Environment of the University of the Witwatersrand, Johannesburg, in fulfilment of the requirements for the degree of Masters of Science in Engineering.

Johannesburg 2018

DECLARATION

I declare that this dissertation is my own unaided work. It is being submitted to the Degree of Master of Science to the University of the Witwatersrand, Johannesburg. It has not been submitted before for any degree or examination to any other University.



…….

(Signature of Candidate)

20th day of June, 2018

ABSTRACT

Improved thermal performance of brakes can be achieved through the redesign of the ventilated core between the two frictional surfaces of disc brakes. A novel wire-woven bulk diamond (WBD) core has shown to increase the cooling performance. This study measured the thermal performance of a solid, pin-finned and WBD disc over a range of speeds simulating a medium-sized truck descending at a constant speed with a fixed braking power input. The braking power was held constant at 2 kW for 3 speeds of 100 rpm, 150 rpm and 250 rpm corresponding to a vehicle speed of approximately 20 km/h, 30 km/h and 50 km/h respectively. The WBD disc was found to reduce the steady state operating temperatures of the braking surface by 5.8%, 8.6% and 16.2% for the operating speeds of 100 rpm, 150 rpm and 250 rpm respectively over those observed for the pin-finned disc; and 4.4%, 12.5% and 32.9% when compared to the solid disc. Finite difference method temperature prediction models were developed for the solid, pin-finned and WBD discs to extend the experimental results to compare the thermal performance of the discs over a wider range of braking powers and speeds and provide insight into the physical interpretation of the experimental results. The temperature prediction models demonstrate a good correlation to the experimental data within 0.46%-3.65% (1.6-13.1 °C). Faster speeds improve the brake disc cooling; the increased cooling with increased rotational speed is more pronounced for the pin-finned disc compared with the solid disc, and most pronounced for the WBD disc. This is because the contribution of the steady state convective heat transfer to the total heat transfer from the ventilated channels of the pin-finned and WBD increases with speed. The convective cooling from the ventilated channel for pin-finned disc is relatively low at ~11% at 50 rpm but increases to ~45.1% at 600 rpm. Similarly, the WBD starts at 50 rpm with a steady state convective heat transfer from the ventilated channel of ~17.1% and increases to ~60.1% at 600 rpm. It was found that at high braking powers, low speeds and short durations the thermal response was primarily influenced by the thermal capacity of the disc whereas at low braking powers, high speeds and longer durations the thermal response is primarily dictated by the cooling capacity of the brake disc.

CONTENTS

DECLARATION i

ABSTRACT ii

CONTENTS iii

NOMENCLATURE v

LIST OF FIGURES vi

LIST OF TABLES viii

1 INTRODUCTION 1

1.1 Background 1

1.2 Significance and Contribution of this Study 2

2 LITERATURE REVIEW 3

3 OBJECTIVE 8

4 EXPERIMENTAL TESTING 9

4.1 Test Specimens 9

4.2 Test Rig 9

4.3 Instrumentation 10

4.4 Test Procedure 11

4.5 Experimental Uncertainty 11

4.6 Experimental Results 12

5 TEMPERATURE PREDICTION MODEL 16

5.1 Finite Difference Method 16

5.2 Heat Transfer from the Outer Surfaces 19

5.3 Heat Transfer from the Ventilated Channels 22

5.4 Model Validation 25

5.5 Understanding the Thermal Response Measurements of Brake Discs at Varying Speeds 29

5.6 Comparison of the Thermal Performance of Solid, Pin-Finned and WBD Discs in Representative Driving Scenarios 34
5.6.1 Emergency braking 34
5.6.2 Urban driving 35
5.6.3 Drag braking 37
6 CONCLUSIONS AND RECOMMENDATIONS 39
7 REFERENCES 41

NOMENCLATURE

Symbol	Description	Units
T_∞	Steady State Surface Temperature	°C
T_{amb}	Ambient Temperature	°C
k	Thermal Conductivity	W/(mK)
ρ	Density	kg/m^3
C_p	Specific Heat	J/(kgK)
ν	Kinematic Viscosity	m^2/s
ε	Emissivity	-
σ	Stephan Boltzmann Constant ($5.67x10^{-8}$ $W/(m^2K^4)$)	$W/(m^2K^4)$
R_0	Inner Hub Radius	m
$R_{i,h}$	Inner Hat Radius	m
$R_{o,h}$	Outer Hat Radius	m
$R_{i,d}$	Inner Disc Radius	m
$R_{o,d}$	Outer Disc Radius	m
l_h	Hat Length	m
l	Rubbing Disc Thickness	m
H	Ventilated Channel Width	m
D_s	Shaft Diameter	m
Gr	Grashof Number	-
β	Coefficient of Thermal Expansion	$°C^{-1}$
g	Gravitational Acceleration (9.81 m/s^2)	m/s^2
$Nu_{Ro,d}$	Nusselt Number (Characteristic Length = $R_{o,d}$)	-
$Re_{Ro,d}$	Reynolds Number (Characteristic Length = $R_{o,d}$)	-
ω	Rotational Velocity of the Disc	rad/s
P	Braking Power	W
m	Disc Mass	kg

LIST OF FIGURES

Figure 1: WBD structure with unit cell highlighted and enlarged [15]. 3
Figure 2: The pin-finned (left) and WBD disc (right) with the inboard rubbing discs replaced with Perspex for display purposes. 3
Figure 3: Area averaged Nusselt number variation with rotational Reynolds number [14]. 4
Figure 4: Mass flow rate of the brake discs tested [14]. 5
Figure 5: Pathlines for a pin-finned rotor (left) and for the flow over a bank of inline cylinders (right) [19]. 5
Figure 6: Relative velocity vector plot at 100 rad/s for the pin-finned disc [21]. 6
Figure 7: The brake testing rig. 10
Figure 8: Experimental results at 100 rpm. 12
Figure 9: Experimental results at 150 rpm. 13
Figure 10: Experimental results at 250 rpm. 14
Figure 11: Experimentally measured surface temperatures at t ≈ 1000±50 s. 14
Figure 12: Experimentally measured surface temperatures at steady state. 15
Figure 13: Finite difference grid. 16
Figure 14: Cross sections through inline rows of pins. 17
Figure 16: FDM models of the solid (a), pin-finned (b) and WBD (c) discs. 18
Figure 15: Rows of pins modelled as concentric cylinders. 18
Figure 17: Schematic of the pin-finned brake disc indicating the predominant energy transfers and key dimensions. 19
Figure 18: Heat transfer correlations for the ventilated channels. 24
Figure 19: Transient results for the solid disc. 25
Figure 20: Transient results at 100 rpm for the solid disc with the predicted results at the lower error bound shown. 26
Figure 21: Transient results for the pin-finned disc. 27
Figure 22: Transient results for the WBD disc. 28
Figure 23: Predicted transient surface temperatures (t = 1000 s) across a range of speeds at a braking power of 2 kW. 30
Figure 24: Transient heat transfers as percentages of the total energy for the solid (a), pin-finned (b) and WBD (c) discs at t = 1000 s and a braking power of 2 kW. 31
Figure 25: Predicted steady state surface temperatures across a range of speed. 32

Figure 26: Steady state heat transfers as percentages of the total energy for the solid (a), pin-finned (b) and WBD (c) discs at a braking power of 2 kW. 33
Figure 27: Temperature rise during a 0.5g braking event from 60 - 0 km/h. 34
Figure 28: Simulated brake cycling from 80 - 20 km/h at a deceleration of 0.3g. 36
Figure 29: Urban braking scenario with +100% convective cooling for the solid disc. 37
Figure 30: Safe drag braking times versus road gradient at 60 km/h. 38

LIST OF TABLES

Table 1: Dimensions and properties of each brake disc. 9

Table 2: Steady state non-dimensional heat transfer data for the external surfaces of each disc. 22

Table 3: Steady state results for the solid disc. 25

Table 4: Steady state results for the pin-finned disc. 27

Table 5: Steady state results for the WBD disc. 28

Table 6: Percent change in peak temperature for the corresponding property change of the solid disc during the emergency braking manoeuvre. 35

Table 7: Percent change in average temperature rise for the corresponding property change of the solid disc during the urban driving scenario. 36

1 INTRODUCTION

1.1 Background

The function of the braking system of a vehicle is to dissipate potential energy given a downhill descent so as to maintain the speed or dissipate kinetic energy so as to bring the vehicle to a halt. This energy is converted into heat which increases the temperature of the braking system components and predominantly the brake disc itself [1, 2]. High temperatures (above 600 °C) are produced during prolonged braking. This can lead to brake fade, thermal distortion, thermal cracking and brake fluid vaporisation, among other detrimental factors [3-6]. These factors deteriorate the braking ability of the vehicle and may lead to brake failure. Extended constant speed downhill descent of heavy vehicles or drag braking can result in highly elevated temperatures due to the constant application of the brakes and the low speed resulting in a low convective cooling coefficient [3]. In these situations brake fade (from excessive brake temperatures) causes a reduced braking ability and may lead to a runaway vehicle. A vehicle of 16 500 kg descending a downhill slope of a 6% incline at 30 km/h may achieve a brake disc surface temperature of 600 °C after 430 s (roughly 7 minutes) neglecting any engine braking, retarder effects or aerodynamic drag [3]. Temperatures exceeding 600 °F (~316 °C) typically exhibit significant brake fade [2].

The convective cooling within the ventilated core of a ventilated brake disc can contribute up to 50%-60% of the overall heat transfer at high rotational speeds whereas at lower speeds it may only contribute a third of the overall heat transfer [7]. Since the operating temperature is a limiting design criterion ventilated brake discs use shaped radial vanes or pins of various cross sections to reduce the maximum operating temperatures by improving the convective cooling [7-11]. Mew *et al*. [12-14] introduced a novel, lightweight brake disc with a wire-woven bulk diamond (WBD) core. The WBD core consists of a lattice of truss-like cells constructed using wire sandwiched between the two rubbing discs [15]. The WBD disc has shown to substantially decrease the operating surface temperature of the brake disc for the continuous downhill braking of a vehicle at a speed of 40 km/h.

1.2 Significance and Contribution of this Study

This study extends the experimental testing at a speed of 40 km/h conducted by Mew *et al.* [12-14] to test at a range of braking speeds to determine the effect of the rotational velocity of the discs (solid, pin-finned and WBD) on the temperature for a given braking power. To achieve this the laboratory rig was improved to allow for more accurate measurement and control of the braking power and speed by automating the testing using a PID controller in conjunction with wireless torque measurements from the shaft. The experimental results from the pin-finned and WBD discs were presented at the Eurobrake Conference in Milan [16]. A finite difference temperature prediction model was developed using heat transfer coefficients obtained from the literature. The lumped parameter first order differential equation used by Mew *et al.* [12-14] provides a good approximation to explain the influence of the thermo-physical parameters which govern the absorption of the braking energy into the disc and its dissipation through a combination of convection, radiation and conduction (modelled using a lumped effective heat transfer coefficient). The developed finite difference model more accurately captures the individual dissipative mechanisms of convection, radiation and conduction; capable of modelling the increased proportion of cooling due to convection at increased rotational speeds. Since a vehicle experiences various braking regimes such as repeated braking in the city, emergency stops, or extended downhill braking [17, 18], and that for each braking mode the disc rotation speed or braking power is different or varies throughout the manoeuvre the model was used to extend the results to an urban driving cycle which could not have been analysed using only the experimental rig on its own.

2 LITERATURE REVIEW

The wire-woven bulk diamond (WBD) brake disc utilises a three-dimensional lattice of steel wire in lieu of traditional ventilated brake disc structures such as solid pins (of varying shapes and sizes) or vanes. This increases the thermal performance of the brake disc and reduces the overall mass of the brake disc while still maintaining structural integrity. The structure is constructed by twisting steel wire into a helical shape and then interweaving the wire at various angles and in various planes into the structure shown in Figure 1 [15]. A brazing material is used to bond the wires together.

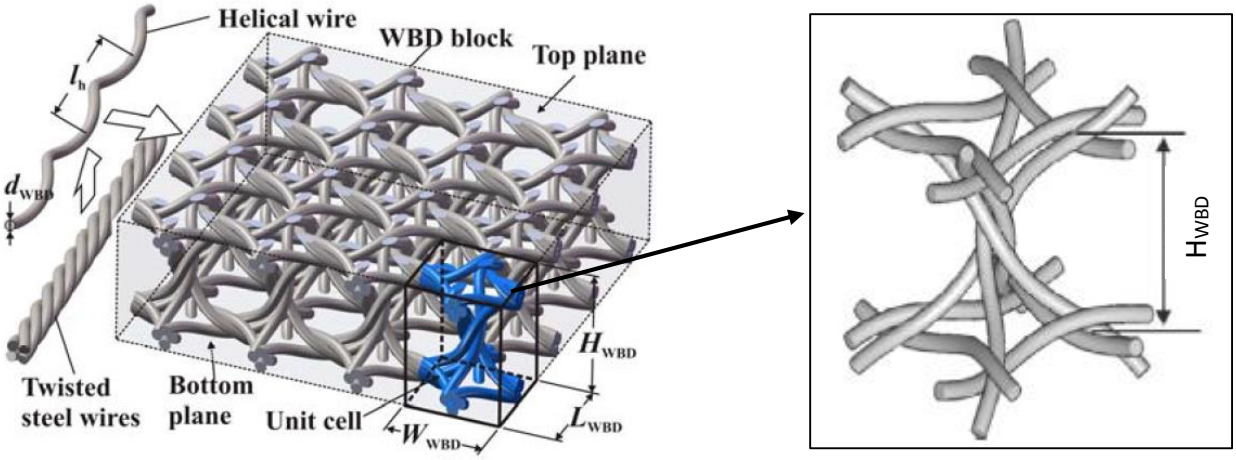


Figure 1: WBD structure with unit cell highlighted and enlarged [15].

The structure is sandwiched between the two rubbing discs and affixed using a brazing agent. Figure 2 shows the internal structures of the pin-finned and WBD discs respectively.

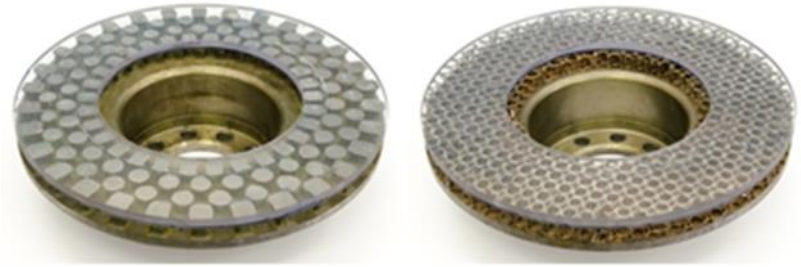


Figure 2: The pin-finned (left) and WBD disc (right) with the inboard rubbing discs replaced with Perspex for display purposes.

Yan *et al*. [14] found that the WBD core reduced the steady state operating temperatures by 16%-36% for a speed range of 100-1000 rpm when compared to an equivalent pin-finned disc. Mew *et al.* [11, 12] found that the WBD disc exhibited a temperature 25% lower than the pin-finned disc which in turn showed a 15% lower temperature than the solid disc at a vehicle speed of approximately 40 km/h. Yan *et al.* [14] determined the variation in area averaged Nusselt number (Nu_{Ro}) with rotational Reynolds number (Re_{Ro}) using the correlation $Nu_{Ro}=CRe_{Ro}^{n}$ for both pin-finned (C = 0.8609 , n = 0.5836) and WBD (C = 0.5776, n = 0.6431) brake discs over a range of rotational speeds (Figure 3). The brake discs were heated using film heating elements affixed to the outer surfaces of the discs to ensure consistent heat flux into the two types of brake disc. The use of heating elements on the outer surface affects the radiation and convective effects from the outer surfaces, but allows for an accurately controlled and repeatable heat flux corresponding to a specific braking power to be generated.

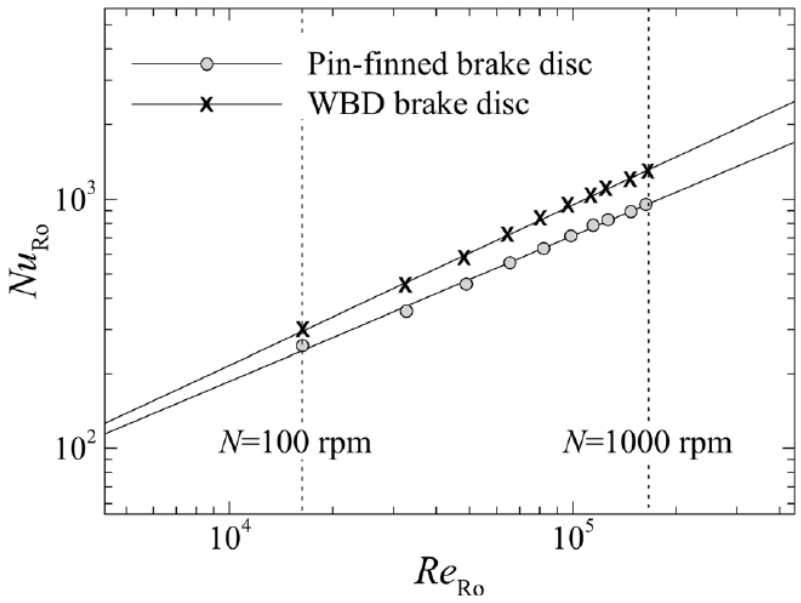


Figure 3: Area averaged Nusselt number variation with rotational Reynolds number [14].

The mass flow rate of the pin-finned and WBD ventilated channels were found to be comparable (Figure 4).

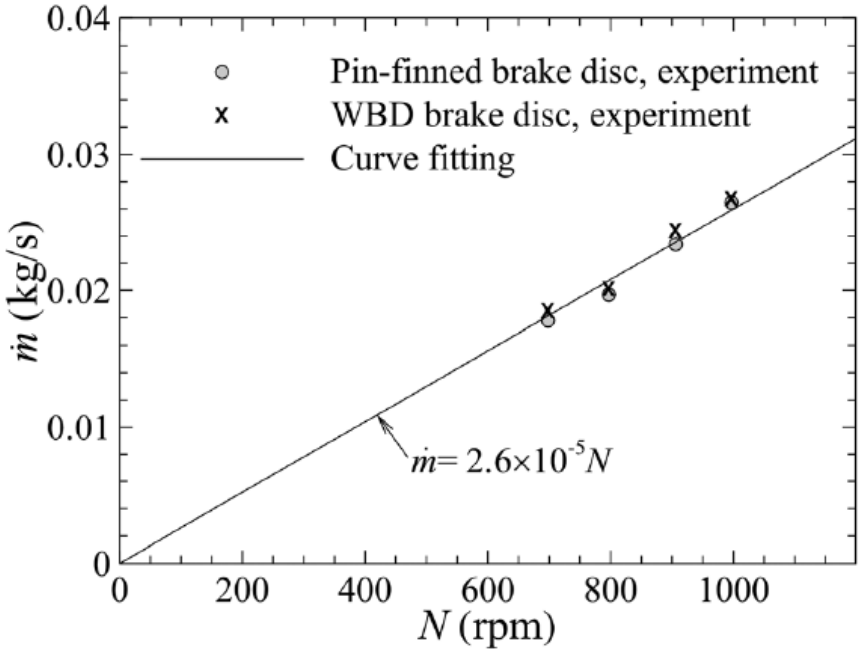


Figure 4: Mass flow rate of the brake discs tested [14].

Palmer *et al*. [19] investigated, using computational fluid dynamics (CFD) , the effects of the first row pin geometry on the flow characteristics of a pin-finned ventilated disc, as well as the effect of changing the geometry of the first row pins has on the overall flow and heat transfer characteristics. Given the radial flow in conjunction with the Coriolis effect the flow

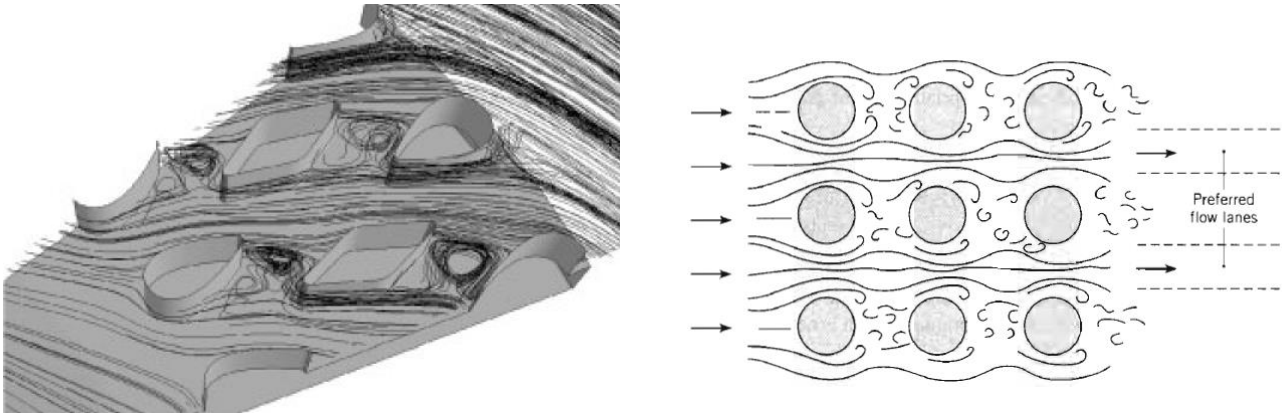


Figure 5: Pathlines for a pin-finned rotor (left) and for the flow over a bank of inline cylinders (right) [19].

within the ventilated channel can be compared to that over an inline bank of cylinders (Figure 5). In this flow regime if the spacing of the pins relative to the flow is such that the ratio of the transverse to the longitudinal spacing of the pins is small the flow will predominantly follow the path of least resistance in lanes between the pins [20]. In essence the upstream pin shields the downstream pin from the majority of the flow detrimentally affecting the local heat transfer [20]. Palmer *et al.* found that decreasing the profile thickness of the front row pins increased the overall mass flow rate and heat transfer [19]. The investigation was undertaken at 500-2000 rpm where convection dominates (radiation and conduction into the hub were neglected), corresponding to 25%-100% of the top speed of a high performance passenger vehicle [19]. A heavy vehicle operates at speeds of 100–600 rpm where radiation and conduction effects are non-negligible.

Wallis *et al*. [21] compared the airflow and heat transfer from three different ventilated designs: straight radial vanes, rounded straight radial vanes and pin-finned design uitilising diamond and teardrop shaped pillars (Figure 6). It was found that the simpler rounded straight radial vane design produced an increased mass flow rate when compared to that of the pin-finned design. However, the heat transfer from these two designs was similar and the authors theorised that the more dispersed material distribution of the pin-finned disc would result in reduced thermal stresses.

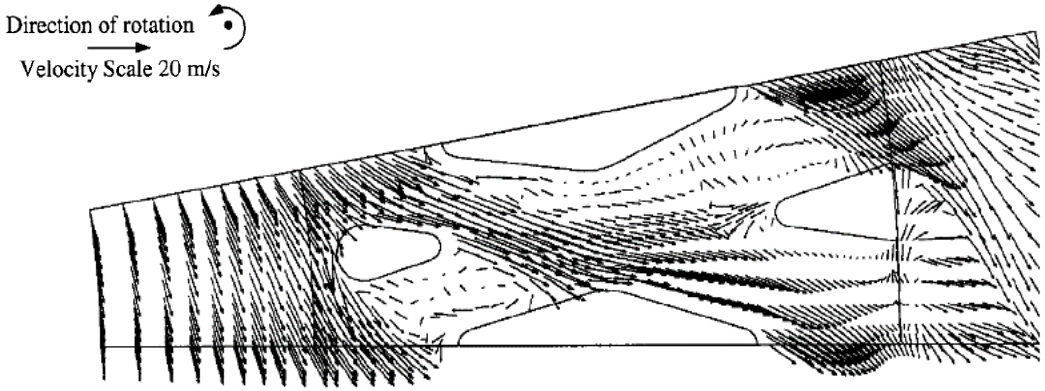


Figure 6: Relative velocity vector plot at 100 rad/s for the pin-finned disc [21].

The preliminary findings pertaining to the WBD brake disc design suggest that: the increased material distribution results in reduced thermal gradients and therefore reduced thermal stresses within the rotor material, the complex arrangement of the WBD core promotes a more tortuous flow path through the ventilated channel (which is advantageous for the overall heat transfer [20]) and the narrow wake production (due to the small frontal area) of the individual elements decreases the local reduction in heat transfer due to the effects depicted in Figure 5 and Figure 6. Given that the WBD design improves the thermal performance of the pin-finned (locally reduced heat transfer in the wake region of the preceding pin) and vaned (low material distribution resulting in increased thermal gradients) brake discs; further investigation into the validity of the WBD design over a broader range of typical braking scenarios is required.

3 OBJECTIVE

The objective of the research was to characterise the thermal response of various brake discs (solid, pin-finned and WBD) at varying speeds.

4 EXPERIMENTAL TESTING

4.1 Test Specimens

Testing was conducted on solid, pin-finned and WBD brake discs compatible for use on a Mercedes Benz Atego 500 series vehicle. The dimensions and properties of each disc are shown in Table 1.

Table 1: Dimensions and properties of each brake disc.

	Solid Disc	Pin-Finned Disc	WBD Disc
Material	Grey Cast Iron	Grey Cast Iron	Mild Steel
Thermal Conductivity (W/mK)	47.8	47.8	43
Specific Heat (J/kgK)	505	505	473
Mass (kg)	18.67	14.22	13.47
Average Emissivity (-)	0.89	0.8	0.8
Ventilated Channel Width (mm)	-	14	14
Rotor Thickness (mm)	-	10	10
Overall Thickness (mm)	34	34	34

4.2 Test Rig

A custom built test rig was used to replicate the braking of a real vehicle. The brake testing rig (Figure 7) consisted of:

1. A 37 kW 3 phase AC motor coupled to a reduction gearbox (3.6:1). The motor speed was controlled using a SEW frequency inverter. The motor has a maximum speed of 1500 rpm (reduced to ~400 rpm at the gearbox output).
2. A flanged shaft onto which the brake discs are mounted. The shaft was coupled to the gearbox using a flexible coupling.
3. A pneumatically actuated brake caliper (Knorr Bremse SN5) with brake booster.
4. A computer controlled Festo proportional pressure regulator (VPPM-C1) to control the braking force applied by varying the pressure supplied to the brakes.
5. A National Instruments CompactRIO microcontroller to control the torque acting on the shaft and by extension the total braking power by controlling the pressure supplied by the pressure regulator. The microcontroller was also used as a data

acquisition system to measure the current input of the non-contact infrared pyrometer.

6. The NI9219 (universal analog input) module which received the strain and temperature signals and the NI9263 (analog voltage output) module which output the pressure control signals.

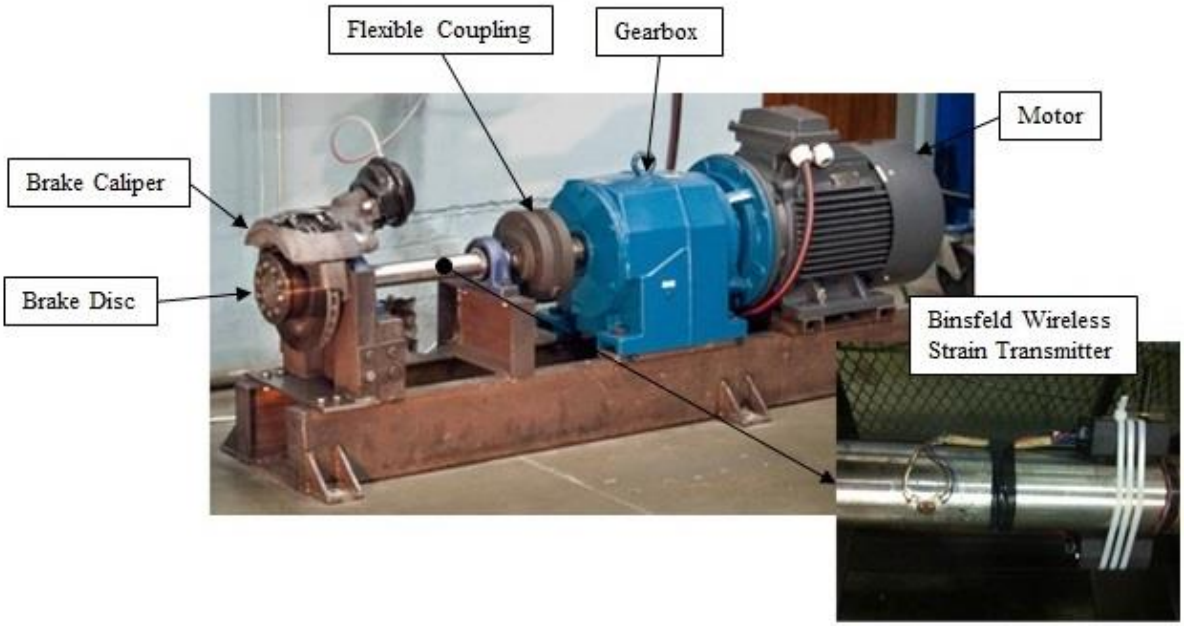


Figure 7: The brake testing rig.

4.3 Instrumentation

The instrumentation consisted of:

1. An Optex Thermo-Hunter non-contact thermometer (CS-30TAC-HT) used to measure the local outboard surface temperatures.
2. A Lord MicroStrain wireless node (SG-Link-OEM-LXRS) and receiver (WSDA-Base-LXRS) used to wirelessly measure the torque of the output shaft via strain gauges mounted thereon. For a number of tests the Lord MicroStrain system was replaced by a Binsfeld TorqueTrack 10k telemetry system as the Lord MicroStrain system needed to be replaced.

4.4 Test Procedure

The research was conducted as follows:

1. The pyrometer was positioned to measure the outboard surface of the disc. The emissivity of each brake disc was determined before each test by heating the brake disc to a temperature of approximately 100 °C and measuring the temperature of the brake discs using a T-type thermocouple and the pyrometer. The temperatures indicated by the pyrometer were then compared to the thermocouple readings and the respective emissivities adjusted until the readings matched those of the thermocouple. This was repeated around the circumference of the disc at the same radius at 8 positions and an average was taken in an attempt to reduce the effect of local emissivity differences. The average emissivities are given in Table 1.

2. Each brake disc was tested at a braking power of 2 kW. The braking power was controlled by monitoring the torque experienced by the shaft (via the strain measurement equipment) and varying the applied braking pressure using a PID algorithm (controlling the output of the Festo pressure regulator) implemented on the compactRIO microcontroller.

3. Each brake disc was tested at 100 rpm, 150 rpm and 250 rpm corresponding to a simulated vehicle speed of approximately 20 km/h, 30 km/h and 50 km/h respectively (assuming a tyre radius of ~0.5 m). The speed was kept constant at the predetermined speed by the SEW frequency inverter. At each speed the discs were allowed to reach steady state in regard to the outboard surface temperatures.

4. Each test was conducted for a duration of ~2¾ hours, which allowed the disc surface temperature to reach steady state.

The brake disc temperatures were continually monitored to ensure that the brake discs did not exceed a temperature of 600 °C to avoid brake failure.

4.5 Experimental Uncertainty

The controlled power was calculated to exhibit an average standard deviation of ~0.19 kW (~9.4%). The Optex Thermo-Hunter non-contact thermometer has a quoted measurement uncertainty of ±1% of reading or ±2 °C, whichever is greater.

4.6 Experimental Results

The experimental results at 100 rpm, 150 rpm and 250 rpm for three disc types tested are given in Figure 8, Figure 9 and Figure 10 respectively. At 100 rpm the pin-finned disc exhibited a steady state surface temperature ~4.8 °C (~1.3%) lower than the solid disc. The WBD brake disc exhibited a surface temperature ~15.3 °C (~4.4%) lower than the solid disc at steady state. Comparatively, at 150 rpm the pin-finned disc was ~11.9 °C (~3.4%) lower at steady state when compared to the solid disc while the WBD was ~39.3 °C (~11.3%) lower. At 250 rpm the pin-finned disc displayed a reduced steady state surface temperature of ~44.1 °C (~12.7%) compared to that of the solid disc whereas the WBD disc demonstrated a reduced surface temperature of ~84.6 °C (~24.3%). The WBD disc showed a reduced steady state surface temperature of ~8.1% (~27.4 °C) at 150 rpm and ~13.3% (~ 40.6 °C) at 250 rpm over those exhibited by the pin-finned disc.

The pin-finned and WBD discs exhibit a steeper gradient in the initial transient phase of the braking application corresponding to a faster increase in the brake disc temperatures when compared to that of the solid brake disc. This is due to the reduced thermal capacity of the pin-finned (mC_p = 7181 J/K) and WBD (mC_p = 6371 J/K) brake discs when compared to that of the solid disc (mC_p = 9428 J/K). The same trend is observed across the speeds tested. Using

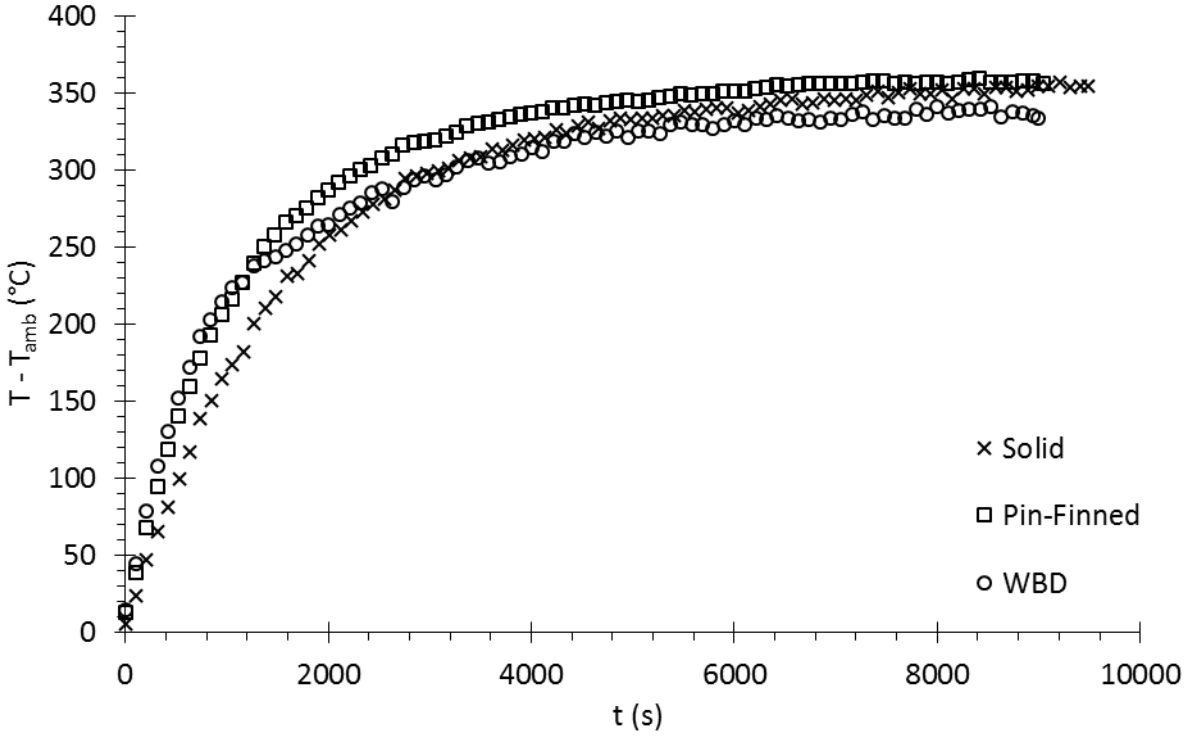


Figure 8: Experimental results at 100 rpm.

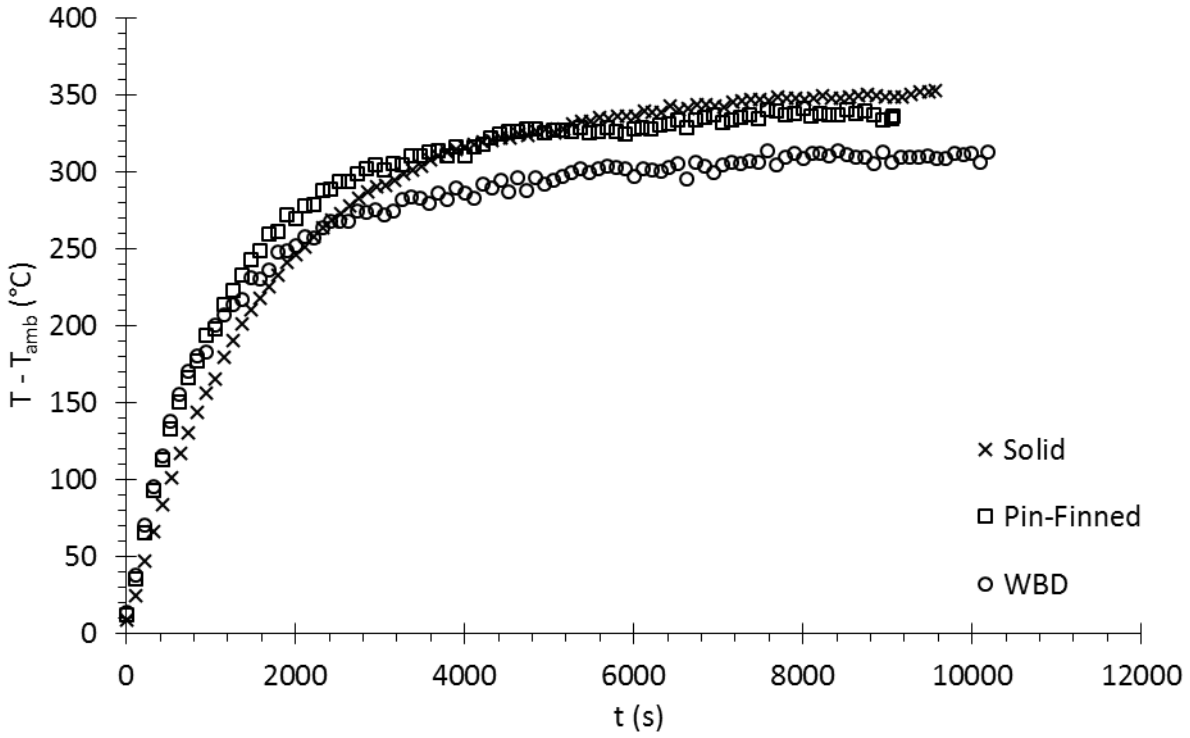


Figure 9: Experimental results at 150 rpm.

a lumped capacitance model it can be shown that the thermal capacity of the brake disc only has an effect on the initial transient performance while the steady state temperature ($t \rightarrow \infty$) is proportional to the effective heat transfer coefficient and area [8].

The large variation in temperature over relatively small time steps in the data for the WBD disc is in part due to the local variation in emissivity around the circumference of the disc, which has been reported by Kasem *et al.* [22].

Figure 11 shows the experimentally measured surface temperatures of each brake disc for each tested speed at $t \approx 1000 \pm 50$ s. At the lower speeds (100 rpm and 150 rpm) the observed trends suggest that the added convective cooling of the ventilated discs is small compared to the energy absorption capabilities at this initial transient phase as indicated by the lower surface temperatures for the solid disc. As the speed is increased to 250 rpm the convective cooling increases for the ventilated discs and has more of an influence on the initial transient temperatures bringing the surface temperatures closer to that of the solid disc.

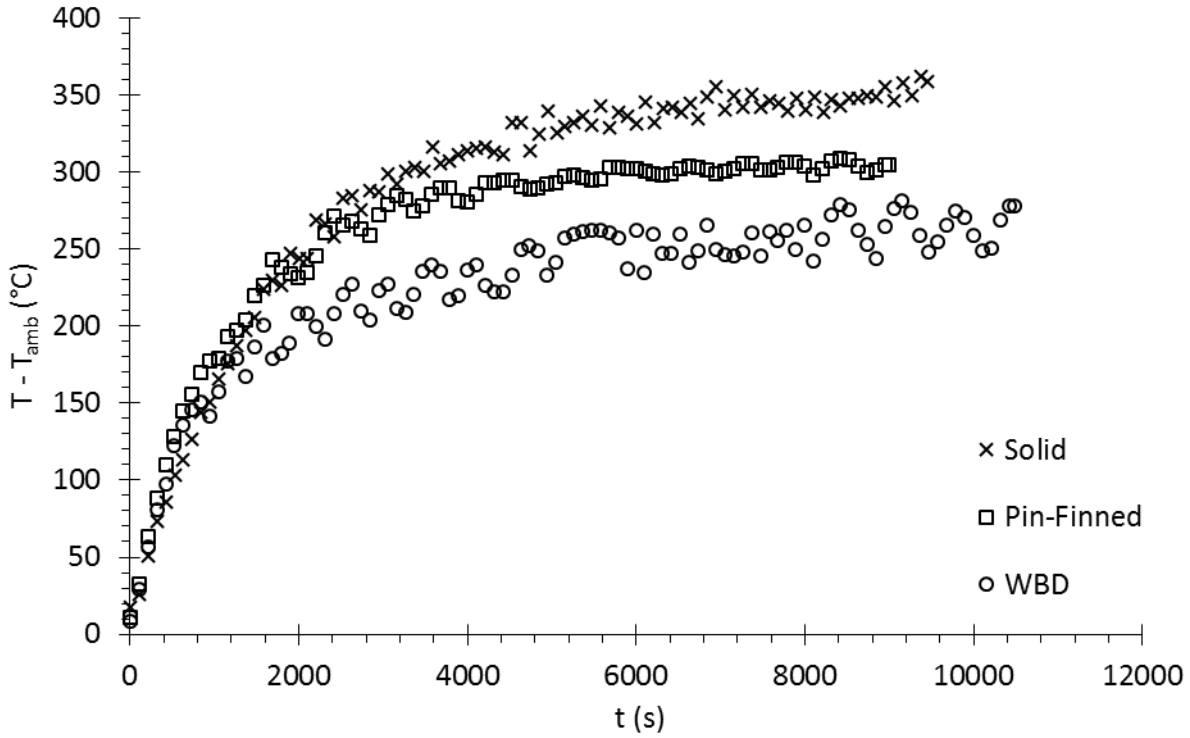


Figure 10: Experimental results at 250 rpm.

Figure 12 shows the experimentally measured steady state surface temperatures of each disc for each tested speed. The steeper negative gradient of the ventilated disc temperatures with respect to speed illustrates that the ventilated discs exhibit improved cooling with speed as compared to the solid disc.

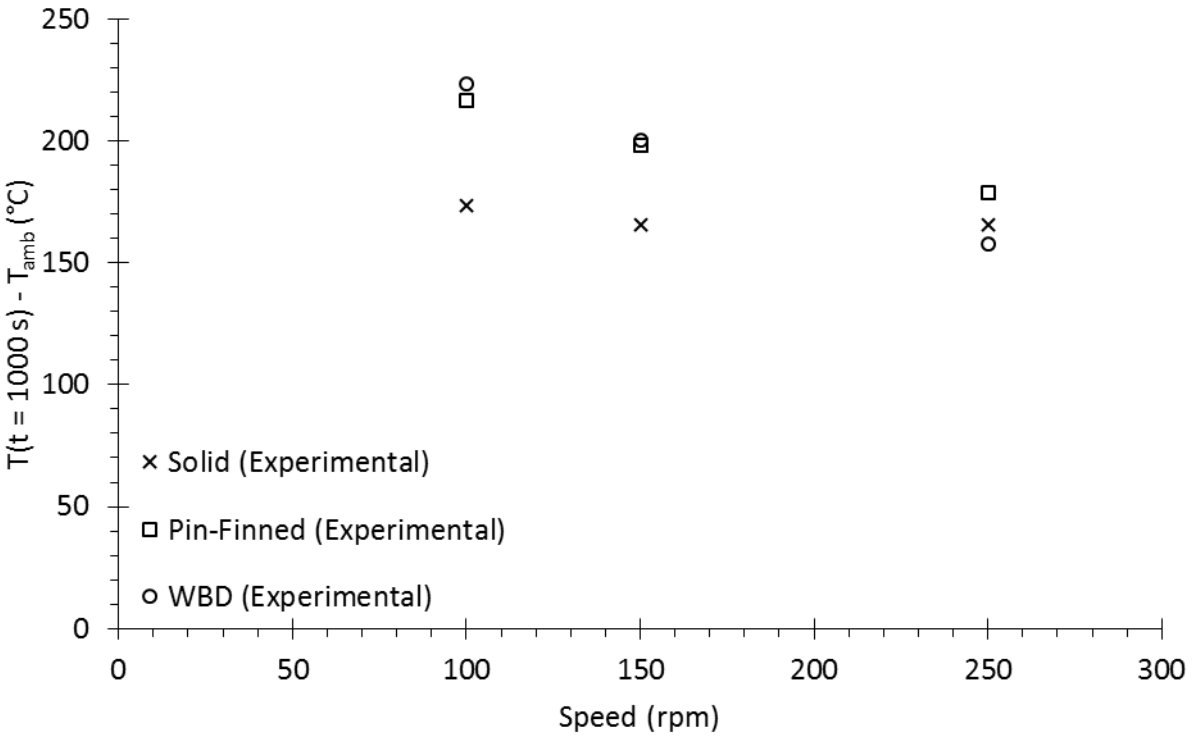


Figure 11: Experimentally measured surface temperatures at t ≈ 1000±50 s.

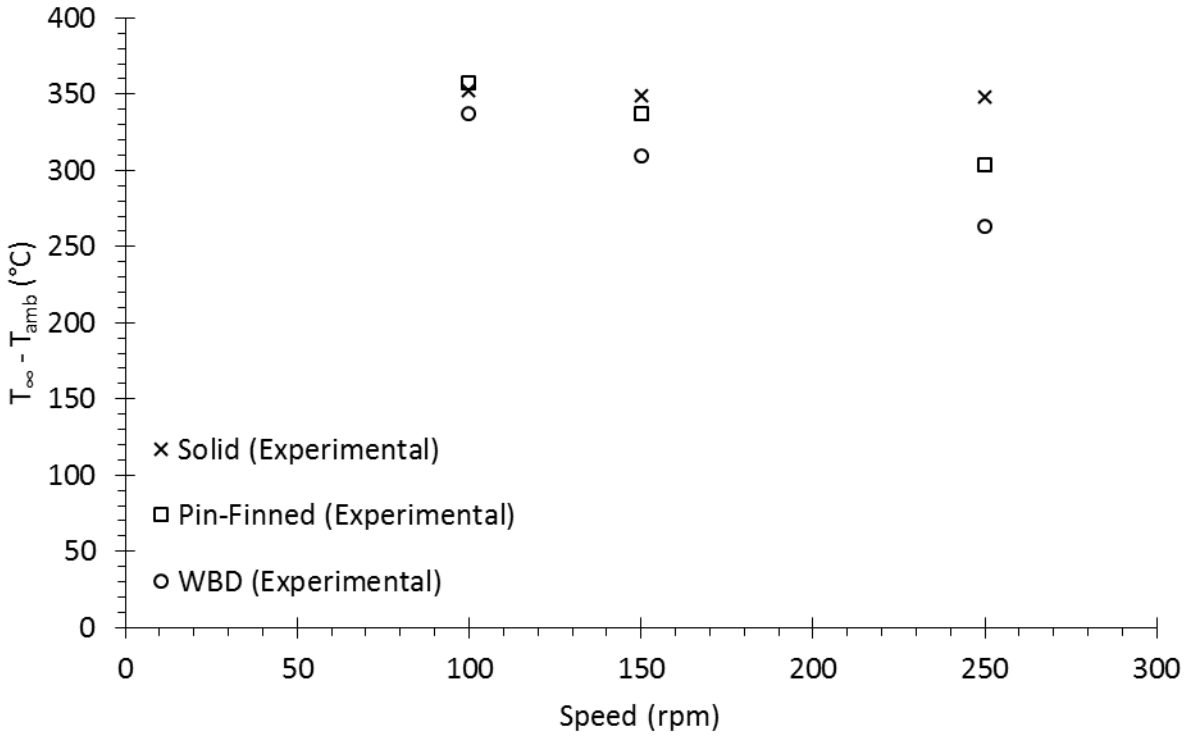


Figure 12: Experimentally measured surface temperatures at steady state.

5 TEMPERATURE PREDICTION MODEL

5.1 Finite Difference Method

A temperature prediction model was developed using the explicit finite difference method (FDM), taking an energy balance over a defined finite element to determine the temperature at the new time step p = p + 1, as outlined by Limpert [2] and Incropera et al. [20]. The model assumes asymmetry, i.e. the temperature of the brake disc does not vary azimuthally (in the angular θ direction). Figure 13 defines the finite difference grid where the z and r-directions represent the dimension through the thickness of the brake disc and the radial dimension respectively. The finite difference grid dimensions Δr and Δz were taken as equal. The nomenclature 'm' and 'n' define the position of the nodes within the z and r - directions respectively whereas 'p' defines the time point where t = pΔt. The surface areas of the respective nodal faces, which vary with radial position, are defined as given in Figure 13.

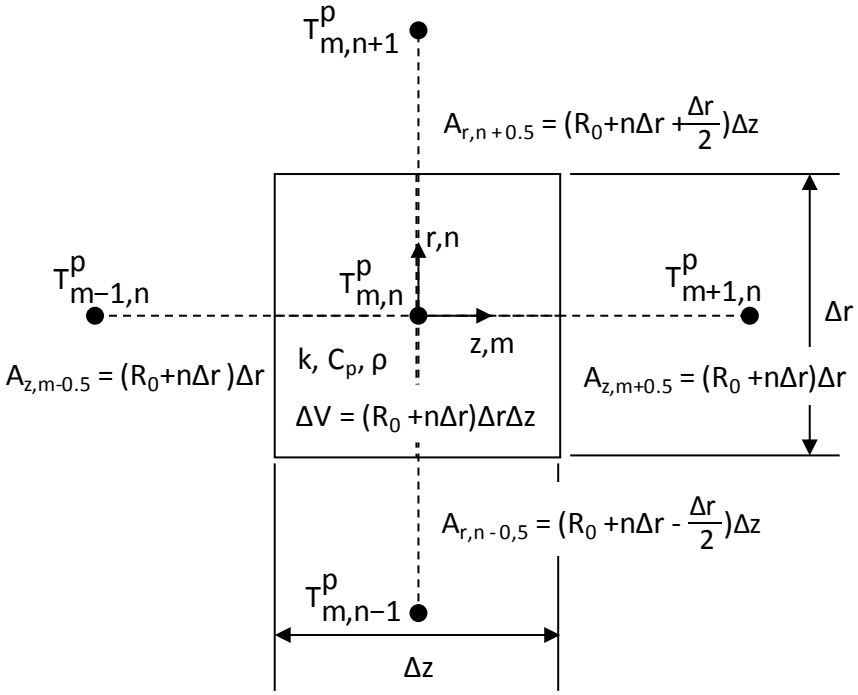


Figure 13: Finite difference grid.

The energy balance taken across the finite element defined in Figure 13 (assuming the energy flow is in the positive directions of the defined axes) is given as:

$$kA_{z,m-0.5}\frac{\left(T^{p}_{m-1,n}- T^{p}_{m,n}\right)}{\Delta z}+kA_{r,n-0.5}\frac{\left(T^{p}_{m,n-1}- T^{p}_{m,n}\right)}{\Delta r}=\rho C_p V\frac{\left(T^{p+1}_{m,n}- T^{p}_{m,n}\right)}{\Delta t}$$
$$+\,kA_{z,m+0.5}\frac{\left(T^{p}_{m,n}- T^{p}_{m+1,n}\right)}{\Delta z}+kA_{r,n+0.5}\frac{\left(T^{p}_{m,n}- T^{p}_{m,n+1}\right)}{\Delta r} \qquad (1)$$

Where $A_{z,m-0.5}$ and $A_{z,m+0.5}$ are the left and right nodal areas normal to the z axis at the nodal point defined by n and m respectively(m^2), $A_{r,n-0.5}$ is the area of the lower surface of the node normal to the r axis (m^2), $A_{r,n+0.5}$ is the area of the upper surface of the node normal to the r axis (m^2), ΔV is the volume of the element used (m^3), k is the thermal conductivity of the material (W/mK), C_p is the specific heat of the material (J/kgK) and ρ is the density of the material (kg/m^3).

Rearranging Equation (1) in terms of the temperature at $t + \Delta t$ $(p + 1)$ and assuming that $\Delta z = \Delta r$ results in:

$$T^{p+1}_{m,n} = T^{p}_{m,n}(1 - 4F_o) + F_o\left\{T^{p}_{m-1,n} + T^{p}_{m+1,n} + T^{p}_{m,n-1} + T^{p}_{m,n+1}\right\} \qquad (2)$$

where $F_o = k\Delta t/\rho C_p(\Delta r)^2$.

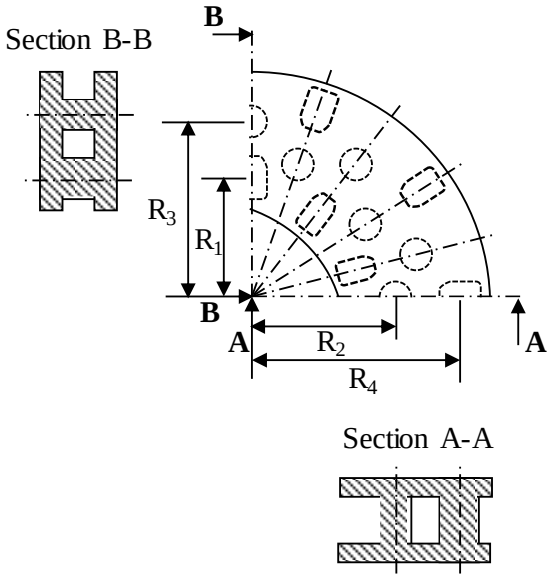


Figure 14: Cross sections through inline rows of pins.

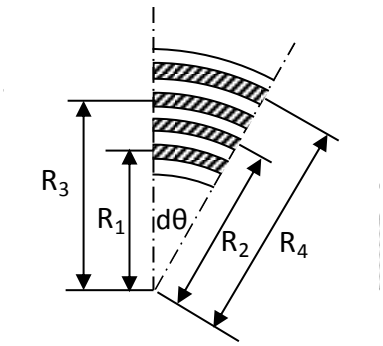
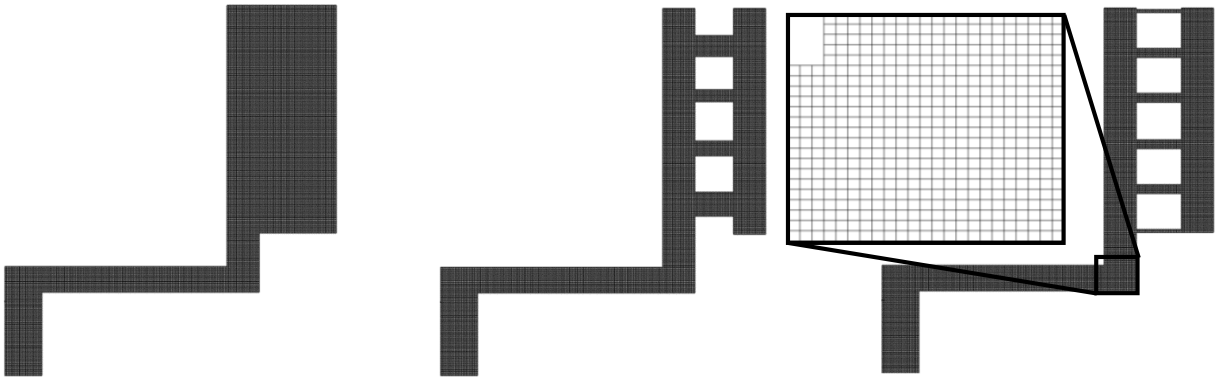


Figure 16: Rows of pins modelled as concentric cylinders.

Following the approach outlined above an expression pertaining to each area of the disc can be formulated, adjusting the above equation to facilitate nodes situated on corners or outer surfaces. The brake temperature problem was modelled using $\Delta r = 0.0005$ m and $\Delta t = 0.005$ s to satisfy the stability criterion ($F_o \leq ¼$) as detailed by [20].

Since the model assumes symmetry in the circumferential direction and the nature of the rows of pins in the ventilated channel is unsymmetrical (as is observed by the varying cross sections depicted in Figure 14), the rows of pins were approximated as annuli (Figure 16). The centreline of each annulus coincided with the radius of the respective row of pins. The thickness of the annuli were determined such that the total surface area and volume (and by extension the total mass) of the brake disc was kept constant. Similarly, the WBD disc was modelled using 6 equally spaced annuli with the thickness equal to 3 mm (corresponding to the thickness of the actual WBD combined ligaments) except for the innermost and outermost layers which were modelled using a thickness of 1.5 mm. To compensate for the extra mass introduced using this assumption the density of the WBD material was reduced to



(a) (b) (c)

Figure 15: FDM models of the solid (a), pin-finned (b) and WBD (c) discs.

7518 kg/m^3 from 7850 kg/m^3. Figure 15 shows the finite element meshes used for each brake disc.

The heat dissipation for each disc was assumed to be through convection and radiation from the outer rubbing disc faces (surface 1) and edges (surface 2), through convection from the ventilated channel (surface 4) and through conduction into the hub (surface 3 in Figure 17).

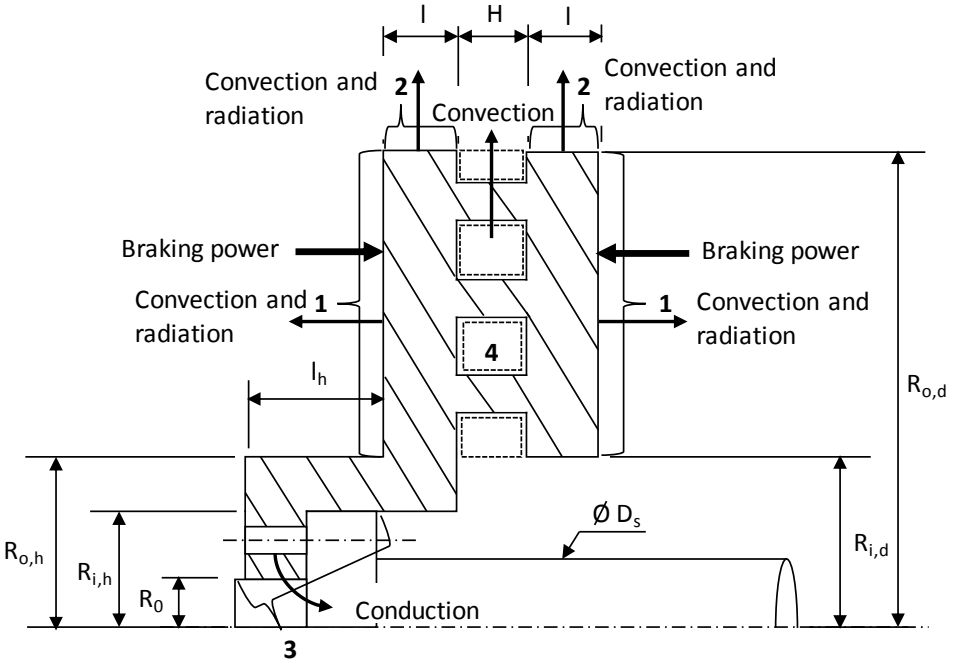


Figure 17: Schematic of the pin-finned brake disc indicating the predominant energy transfers and key dimensions.

5.2 Heat Transfer from the Outer Surfaces

The heat transfer (h_d) from surface 1 was approximated using the correlation for an isolated disc rotating in still air with laminar flow ($Re_{Ro} < 180\,000$). Given the initial low speeds of the tests ($1.96 \times 10^4 < Re_{Ro} < 4.89 \times 10^4$) an expression including the effects of natural convention (Grashof number) was required [23]:

$$\left(Nu_{R_{o,d}}\right)_d = \frac{h_d R_{o,d}}{k_{air}} = 0.4\left(Re_{R_{o,d}}^2 + Gr\right)^{0.25} \quad (3)$$

The rotational Reynolds number is given as:

$$Re_{R_{o,d}} = \frac{\omega R_{o,d}^2}{\nu_{air}} \tag{4}$$

where ω is the rotational velocity of the disc in rad/s and R_o is the outer disc radius in m.

The Grashof number is defined as:

$$Gr = \frac{gD^3\beta(T-T_{amb})}{\nu_{air}^2} \tag{5}$$

where g is the acceleration due to gravity in m/s^2, β is the coefficient of thermal expansion °C^{-1} and D is the diameter in m.

The heat transfer coefficient (h_e) from the disc edges (surface 2 in Figure 17 was approximated using the correlation for a rotating cylinder with or without crossflow [10]:

$$\left(Nu_{R_{o,d}}\right)_e = \frac{h_e R_{o,d}}{k_{air}} = 0.06\left(2Re_{R_{o,d}}^2 + 4Re_t^2\right)^{0.33} \tag{6}$$

where Re_{Ro} is defined as per Equation (4) and Re_t is the transverse Reynolds number which is taken as $Re_t = 0$ for no crossflow.

The radiative heat transfer from surfaces 1 and 2 was given as:

$$Q_{rad} = \sigma\varepsilon A(T^4 - T_{amb}^4) \tag{7}$$

where σ is the Stephan Boltzmann constant (5.67x10^{-8} W/(m^{2}K^4)), ε is the emissivity and A is the surface area associated with the radiative heat transfer in m^2.

The heat transfer coefficient from the outer surface of the driven shaft was approximated as that for a cylinder rotating in still air due to the low operating range of the Reynolds number (inclusive of natural convection effects) [24]:

$$\left(Nu_{D_s}\right)_s = 0.11\left(0.5Re_{D_s}^2 + GrPr\right)^{0.35} \qquad Re_{D_s} > 8000 \tag{8}$$

The rotational Reynolds number (with characteristic length D_s) is given as:

$$Re_{D_s} = \frac{\pi \omega D_s^2}{\nu_{air}} \tag{9}$$

where D_s is the outer diameter of the shaft in m and ν_{air} is the kinematic viscosity of air in m^2/s.

The Nusselt number is given as:

$$\left(Nu_{D_s}\right)_s = \frac{h_s D_s}{k_{air}} \tag{10}$$

where h_s is the convective heat transfer coefficient associated with the shaft in W/m^2K and k_{air} is the thermal conductivity of air in W/mK.

The driven shaft was modelled as a fin with a length of 1 m (the tip temperature equal to the ambient temperature). The average conduction into the hub (surface 3 in Figure 17) was given as:

$$Q_s = \frac{\sqrt{h_s p k_{steel} A_s}}{\tanh\left(\sqrt{\frac{h_s p}{k_{steel} A_s}}\right)} (T_b - T_{amb}) \tag{11}$$

where p is the perimeter of the shaft in m and A_s is the cross sectional area of the shaft in m^2. The convective heat transfer coefficient (h_s) was approximated as per Equation (8)-(10). The base temperature T_b was approximated as the average temperature of surface 3 in Figure 17.

Table 2 summarises the steady state non-dimensional heat transfer results using the experimental results in conjunction with the above equations for each speed and disc tested. Columns 2-5 correspond to Equations (4), (9), (6), (3) and (8) respectively.

Table 2: Steady state non-dimensional heat transfer data for the external surfaces of each disc.

	Speed (rpm)	$Re_{Ro,d}$ (-)	Re_{Ds} (-)	$(Nu_{Ro,d})_e$ (-)	$(Nu_{Ro,d})_d$ (-)	$(Nu_{Ro,d})_s$ (-)
Solid	100	1.96×10^4	7.84×10^3	51.3	88.1	47.9
	150	2.93×10^4	1.18×10^4	67.0	92.1	62.2
	250	4.89×10^4	1.96×10^4	93.9	102.6	87.8
Pin-Finned	100	1.96×10^4	7.84×10^3	51.3	88.3	47.9
	150	2.93×10^4	1.18×10^4	67.0	91.6	62.1
	250	4.89×10^4	1.96×10^4	93.9	101.2	87.7
WBD	100	1.96×10^4	7.84×10^3	51.3	87.3	47.8
	150	2.93×10^4	1.18×10^4	67.0	90.3	62.1
	250	4.89×10^4	1.96×10^4	93.9	99.7	87.7

The heat transfer coefficient for the inboard disc face rotating in close proximity to the caliper mounting structures was modelled using the correlation for the relative heat transfer from the shrouded side of a rotating disc in Richardson *et al.* [23]. Using the ratio of disc diameter to gap width as ~15 the relative heat transfer for the inboard face can be approximated as ~$0.8h_d$ [23]. To take into account the caliper covering the disc outer edges a factor of 0.8 was approximated to reflect the reduction in effective surface area. Additionally the disc outer surface area was reduced by a factor of $1\text{-}A_{pad}/A_{disc} \approx 0.82$, where A_{pad} is the surface area covered by the brake pad (~ 0.0113 m^2).

5.3 Heat Transfer from the Ventilated Channels

Using the steady state temperature data from Yan *et al.* [14] correlated with the experimental data from the current study the convective heat transfer for the ventilated channels (surface 4 in Figure 17) of the WBD and pin-finned discs was approximated using the lumped formulation:

$$T(t)\text{-}T_{amb} = \frac{P}{(hA)_{eq}}\left(1\text{-}e^{-\frac{(hA)_{eq}}{mC_p}t}\right) \tag{12}$$

At steady state ($t \rightarrow \infty$) the expression becomes:

$$T_\infty\text{-}T_{amb} = \frac{P}{(hA)_{eq}} \tag{13}$$

The term $(hA)_{eq}$ denotes an equivalent factor equal to the sum of the individual heat transfers:

$$(hA)_{eq}=h_vA_v+ (h_d+h_r)A_d+ (h_e+h_r)A_e+ \frac{\sqrt{h_spk_{steel}A_s}}{\tanh\left(\sqrt{\frac{h_sp}{k_{steel}A_s}}\right)} \quad (14)$$

Rearranging Equation (13) and (14) in terms of the heat transfer coefficient of the ventilated channel (h_v) at a given rotational speed:

$$h_v = \frac{1}{A_v}\left\{\frac{P}{T_\infty-T_{amb}} - \left[(h_d+h_r)A_d+ (h_e+h_r)A_e + \frac{\sqrt{h_spk_{steel}A_s}}{\tanh\left(\sqrt{\frac{h_sp}{k_{steel}A_s}}\right)}\right]\right\} \quad (15)$$

where h_d is the convective heat transfer coefficient of the disc faces (modelled using Equation (3) in conjunction with the experimental steady state data in Table 2) in W/(m^{2}K), h_s is the convective heat transfer coefficient of the shaft (modelled using Equation (8) in conjunction with the experimental steady state data in Table 2) in W/(m^{2}K), h_e is the convective heat transfer from the disc edges (modelled using Equation (6) in conjunction with the experimental steady state data in Table 2) in W/m^{2}K and h_r is the radiative heat transfer coefficient ($h_r = \sigma\varepsilon(T^4 – T_{amb}^4)/(T – T_{amb})$) in W/(m^{2}K). A_v, A_d and A_e are the total vent area, the disc outer surface area and the disc edge surface area respectively in m^2.

The Nusselt number correlations using the heat transfer coefficient found with Equation (15) and related to the rotational Reynolds number are shown in Figure 18. The results indicate an improved convective heat transfer for the WBD disc over the pin finned disc, with a corresponding improvement with increasing Reynolds number.

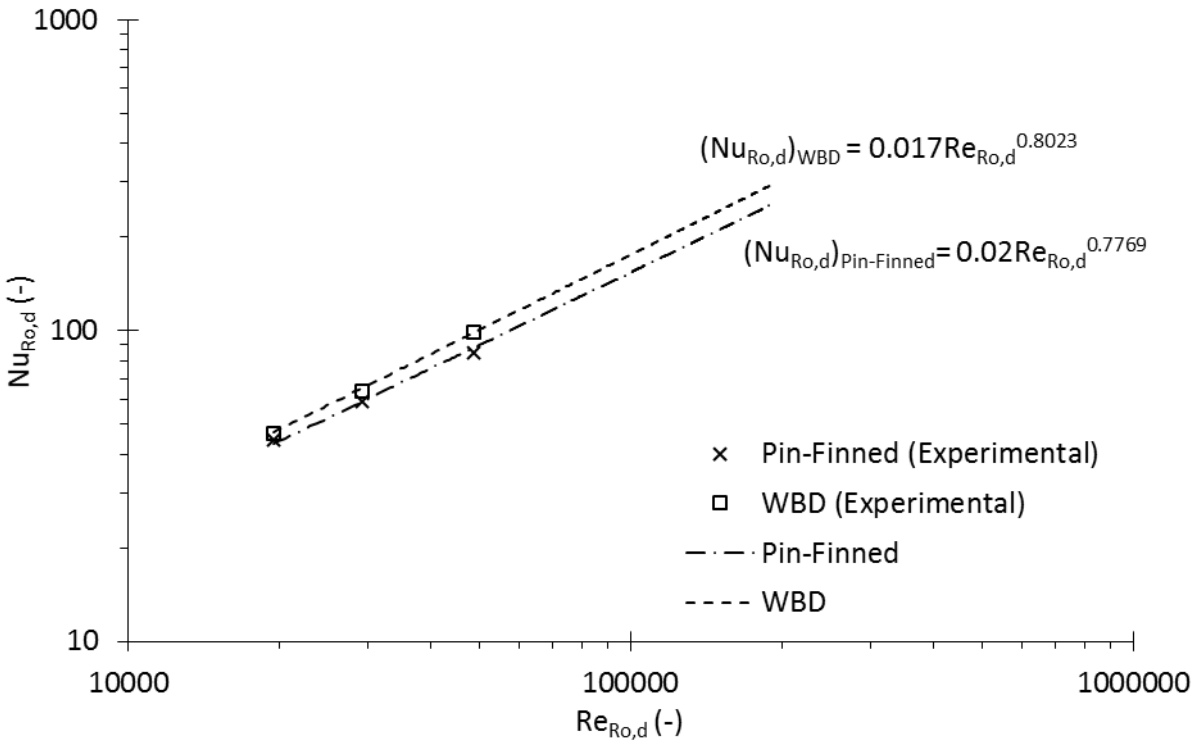


Figure 18: Heat transfer correlations for the ventilated channels.

Using the correlations above in conjunction with the finite difference method the temperature at each nodal point (Figure 15) over time of each brake disc can be predicted for a given braking power and speed. From this the surface temperatures can be extracted and compared to those measured experimentally. Furthermore the contribution of each heat transfer component can be more accurately predicted than for that of a lumped capacity method.

5.4 Model Validation

The predicted temperature increases of the solid disc (at 100 rpm, 150 rpm and 250 rpm) at a braking power of 2 kW are shown as lines and compared with the experimental results, given as points, in Figure 19. The temperature prediction model shows good correlation with a maximum steady state difference of 3.65% (~13.1 °C) at 100 rpm (Table 3).

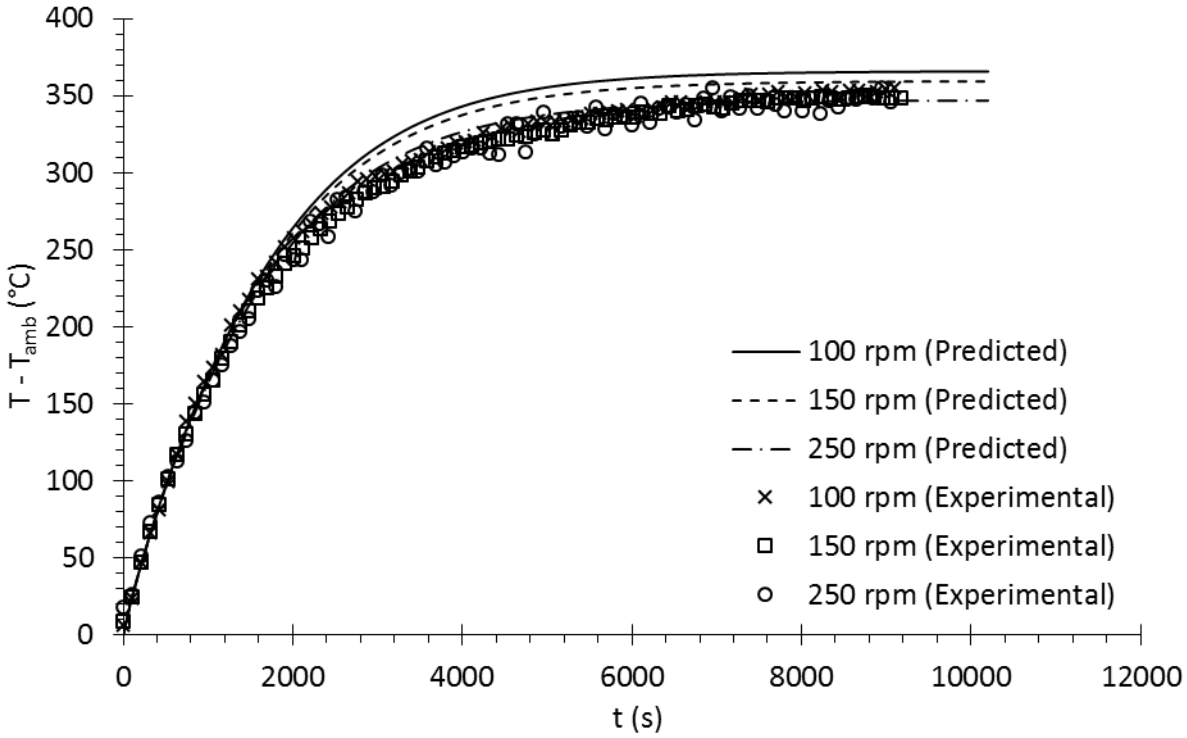


Figure 19: Transient results for the solid disc.

Table 3: Steady state results for the solid disc.

Speed (rpm)	Experimental Steady State Temperature (°C)	Predicted Steady State Temperature (°C)	Steady State Difference (°C)	Steady State Difference (%)
100	352.3	365.4	13.1	3.65
150	349.1	358.8	9.7	2.74
250	347.9	346.3	1.6	0.46

The largest difference between the predicted results and the experimental results (Figure 19) occurs between roughly t = 2000 s and t = 6000 s. Figure 20 shows the predicted results at the lower error bound of the experimentally controlled power (2±0.19 kW), the figure illustrates that the error in controlling the experimentally controlled power is a possible explanation for this difference. Other possible sources of the difference are the fact that the heat transfer coefficients used in the model are for discs and cylinders with no hat attachments as is the case for a brake disc. Furthermore, the prediction model assumes that the braking power is all absorbed and dissipated by the disc. A small but significant portion of the braking power is absorbed by the brake pads and caliper.

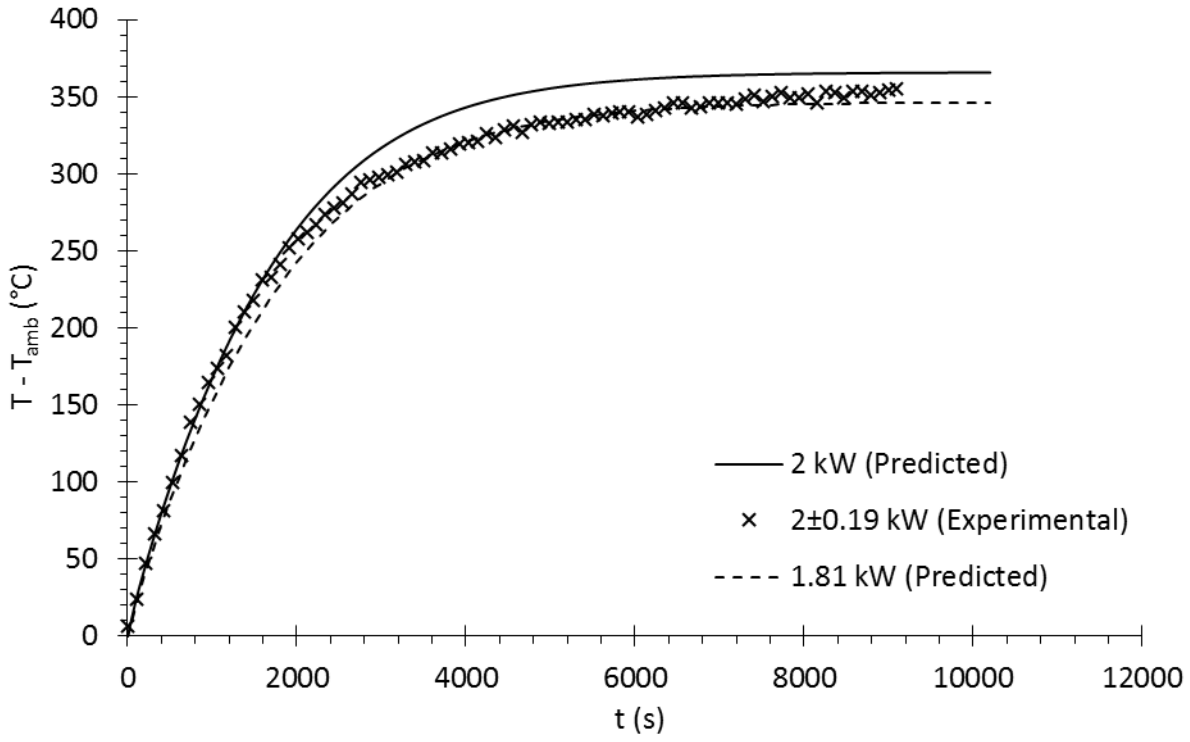


Figure 20: Transient results at 100 rpm for the solid disc with the predicted results at the lower error bound shown.

The predicted temperature increases of the pin-finned disc (at 100 rpm, 150 rpm and 250 rpm) at a braking power of 2 kW are shown as lines and compared with the experimental results, given as points, in Figure 21. The temperature prediction model shows good correlation with a maximum steady state difference of 1.60% (~4.8 °C) at 250 rpm (Table 4).

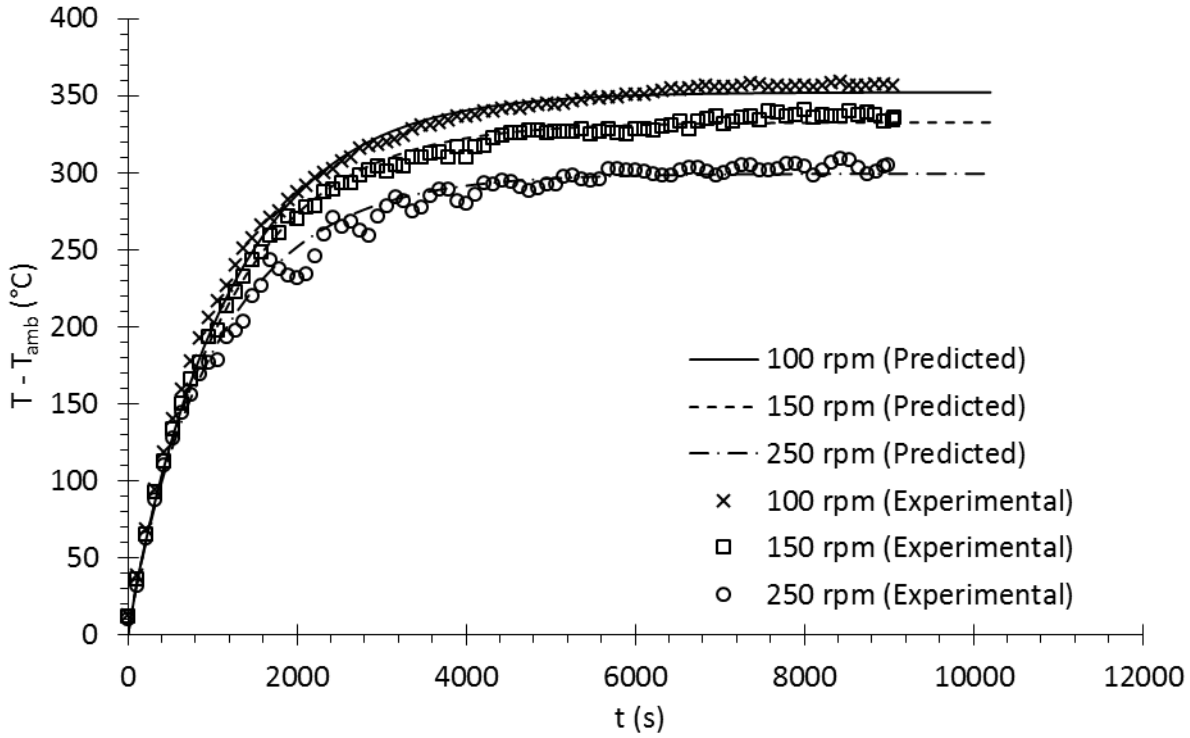


Figure 21: Transient results for the pin-finned disc.

Table 4: Steady state results for the pin-finned disc.

Speed (rpm)	Experimental Steady State Temperature (°C)	Predicted Steady State Temperature (°C)	Steady State Difference (°C)	Steady State Difference (%)
100	357.1	352.0	5.0	1.42
150	337.2	332.4	4.8	1.44
250	303.8	299.0	4.8	1.60

The predicted temperature increases of the WBD disc (at 100 rpm, 150 rpm and 250 rpm) at a braking power of 2 kW are shown as lines and compared with the experimental results, given as points, in Figure 22. The temperature prediction model shows good correlation with a maximum steady state difference of 2.24% (~6.9 °C) at 150 rpm (Table 5). There is a larger difference between the model and experimental results in the transitional phase (between t ≈ 1000 s and t ≈ 3000 s) as compared to the steady state differences; the model predicts a temperature of ~235 °C at t = 2000 s at 250 rpm compared to the experimental measurement of ~208 °C.

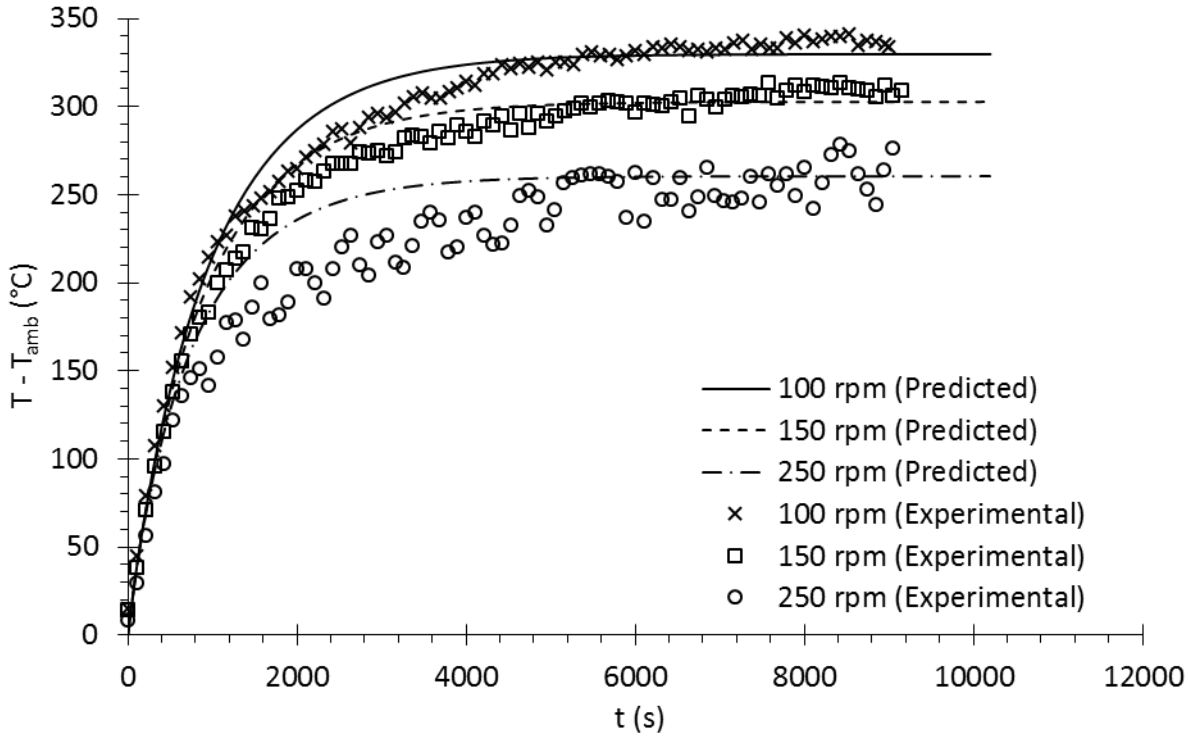


Figure 22: Transient results for the WBD disc.

Table 5: Steady state results for the WBD disc.

Speed (rpm)	Experimental Steady State Temperature (°C)	Predicted Steady State Temperature (°C)	Steady State Difference (°C)	Steady State Difference (%)
100	337.0	329.7	7.3	2.19
150	309.9	303.0	6.9	2.24
250	263.4	260.2	3.2	1.23

The model was deemed to have an acceptable degree of accuracy when considering that the experimental results have a measurement error, the model does not account for a small but significant portion of the braking power going into the brake pads and the heat transfer correlations used pertain to simplified geometries which do not account for all the effects that the hub or caliper may have on the flow and therefore heat transfer over the rotor faces.

5.5 Understanding the Thermal Response Measurements of Brake Discs at Varying Speeds

Figure 11 and Figure 23 show the experimentally measured and the predicted transient temperatures at t = 1000 s, and a braking power of 2 kW, respectively. The solid disc is predicted to have lower surface temperature up to ~450 rpm when compared to the WBD disc and up to ~600 rpm when compared to the pin-finned disc. The pin-finned disc is predicted to have a lower surface temperature up to ~300 rpm when compared to the WBD disc. Figure 24 shows the heat dissipated through conduction, convection through the outer surfaces, convection through the ventilated channel, radiation and absorbed (stored) in the disc as a percent of the total braking energy for each disc at t = 1000 s and a braking power of 2 kW. During this transient phase the predominant energy transfer is absorption across the range of speeds for the solid disc (71.9%-59.5%).The energy absorption of the pin-finned disc is dominant up to ~580 rpm. The energy absorption of the WBD disc is dominant only up to ~250 rpm (49.6%-32%) after which the convective cooling from the channel dominates (up to 51% at 600 rpm). The improved performance of the WBD disc when compared to the pin-finned disc in this regard may be due to the larger mass of the pin-finned disc (resulting in a higher energy absorption capacity) and the smaller ventilated channel surface area and associated heat transfer coefficient (resulting in a lower overall heat transfer capability from the ventilated channel).The convection form the outer surfaces, radiation and conduction into the hub show similar values across the range of speeds when comparing each disc. Since the solid disc exhibits more mass the energy absorbed results in a lower temperature than for that of the pin-finned or WBD discs. At the higher speeds (greater than ~450 rpm) when the convective cooling from the WBD ventilated channel becomes sufficiently high relative to the energy stored (~45% and ~22% respectively at 450 rpm) the WBD starts to produce lower surface temperatures when compared to the solid disc. The pin-finned disc only starts to

exhibit greater heat transfer from the ventilated channel relative to the energy stored after ~600 rpm which is the cross over point with the solid disc in Figure 23.

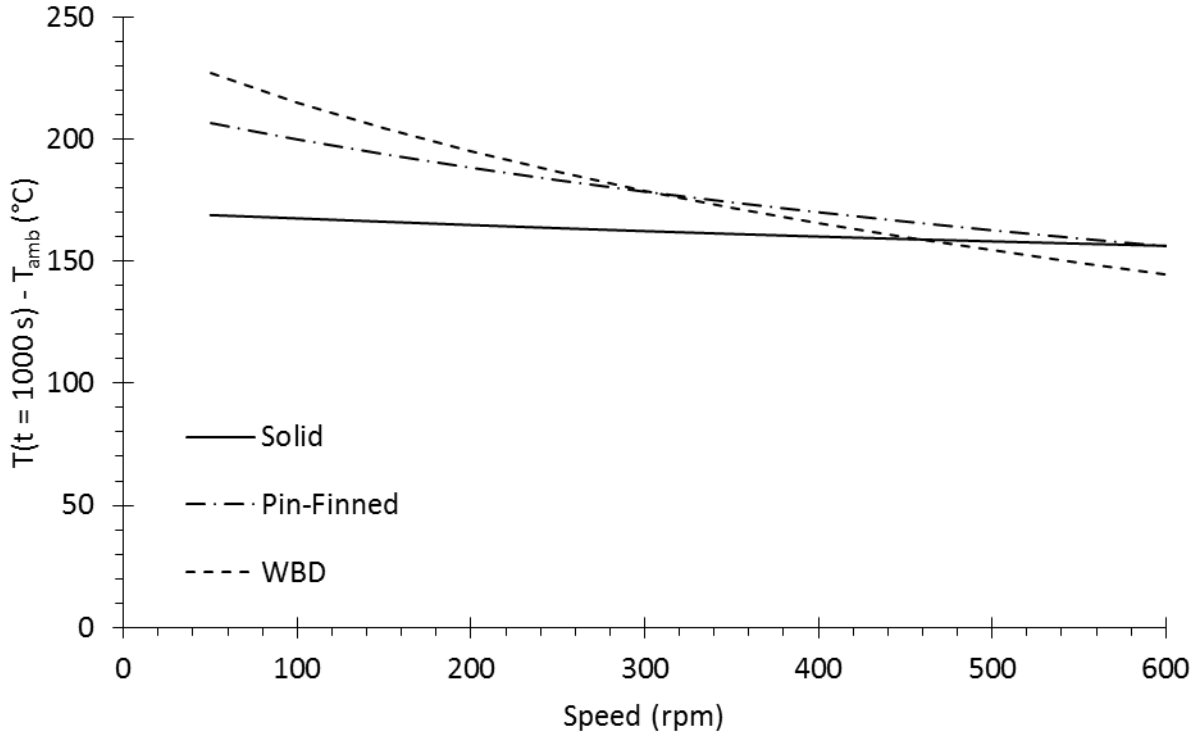


Figure 23: Predicted transient surface temperatures (t = 1000 s) across a range of speeds at a braking power of 2 kW.

Figure 12 and Figure 25 show the experimentally measured and the predicted steady state temperatures at a braking power of 2 kW. The ventilated brake discs exhibit reduced steady state surface temperatures across the range of speeds (with the only exception being for the pin-finned disc at 50 rpm) when compared to the solid disc. The predicted difference between the pin-finned and WBD disc ranges from ~13 °C (~3.5%) to ~47 °C (~21.2%) from 50 rpm to 600 rpm respectively. However, the difference plateaus at ~500 rpm at ~47 °C.

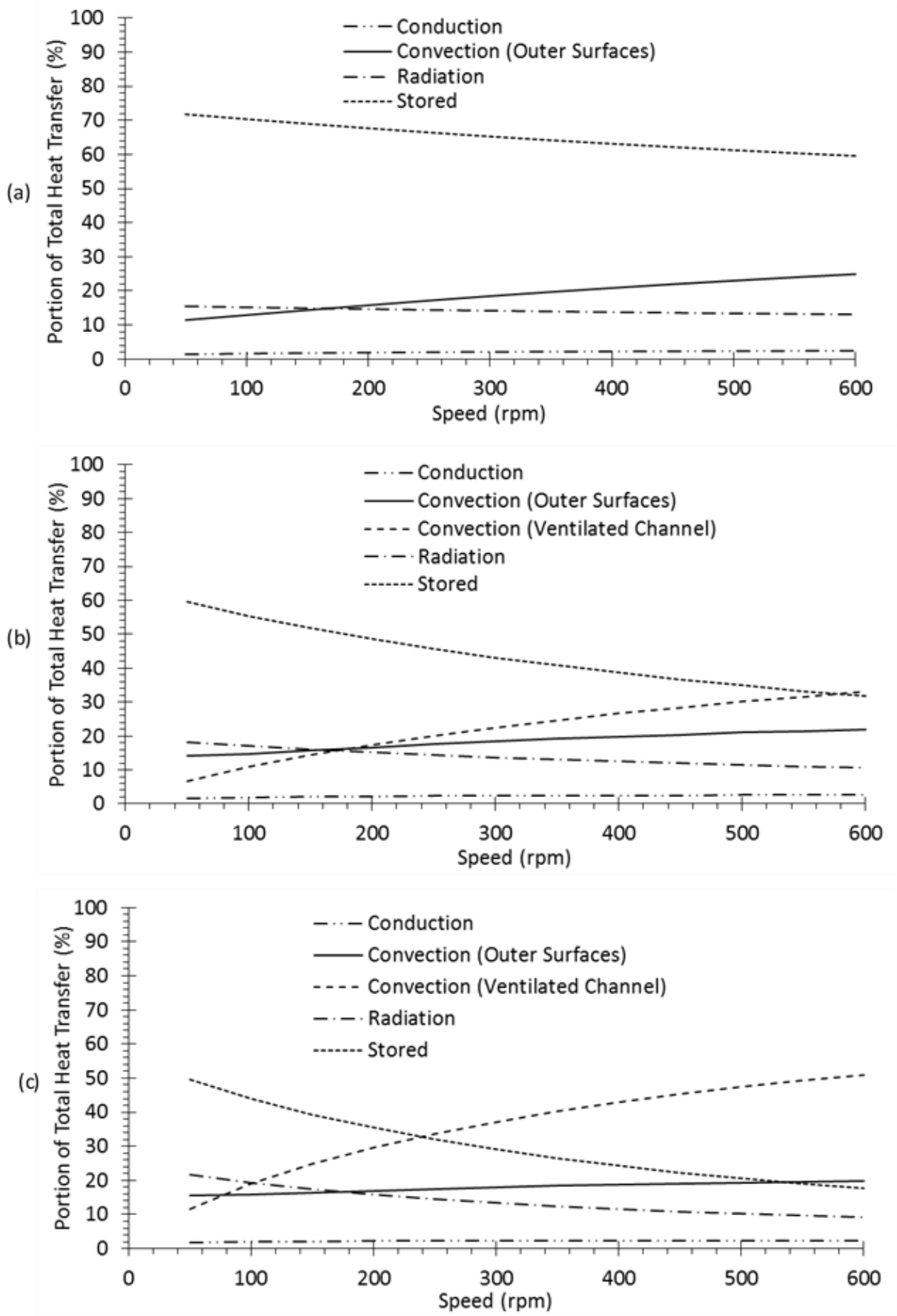


Figure 24: Transient heat transfers as percentages of the total energy for the solid (a), pin-finned (b) and WBD (c) discs at t = 1000 s and a braking power of 2 kW.

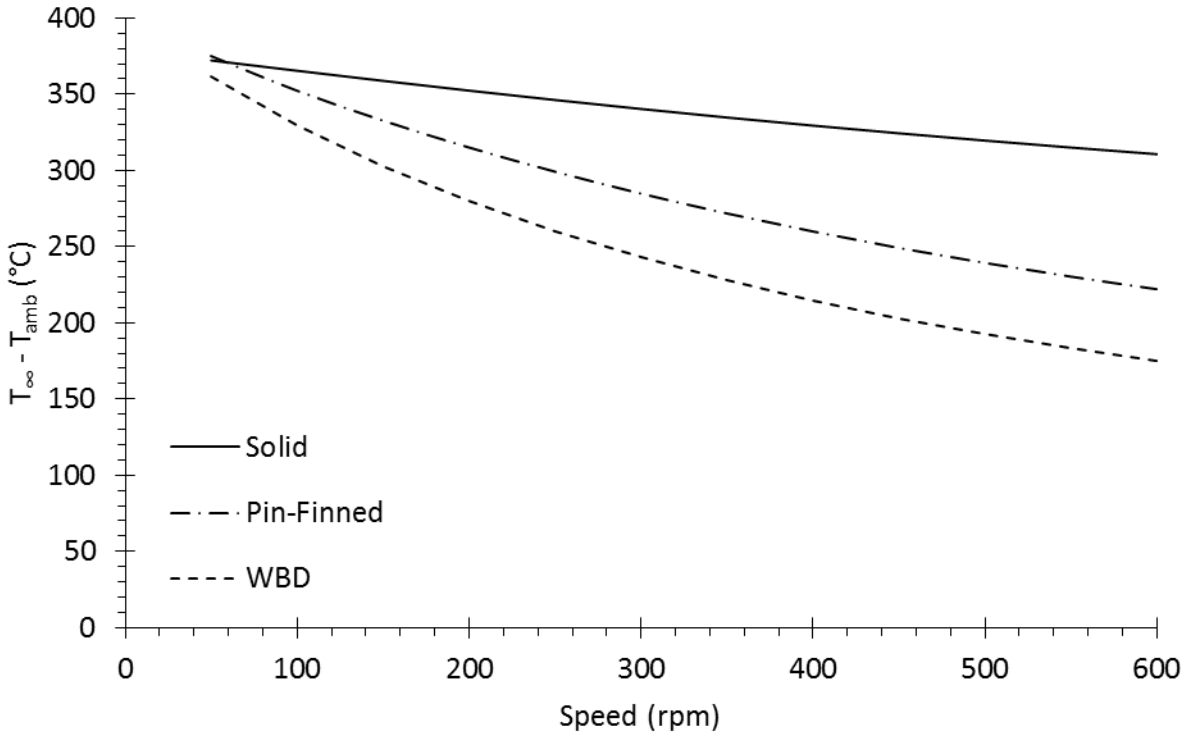


Figure 25: Predicted steady state surface temperatures across a range of speed.

Figure 26 shows the heat dissipated through conduction, convection through the outer surfaces, convection through the ventilated channel and radiation as a percent of the total braking energy for each disc at a braking power of 2 kW. The dominant steady state energy dissipation mechanism of the solid disc is radiation contributing as much as ~68% at 50 rpm down to ~45.6% at 600 rpm. The convective mechanism increases from ~26.9% at 50 rpm to ~46.6% at 600 rpm. The steady state convective heat transfer from the ventilated channel of the pin-finned disc starts out relatively low at ~11% at 50 rpm but increases to ~45.1% at 600 rpm. Similarly, the WBD exhibits a steady state convective heat transfer from the ventilated channel of ~17.1% at 50 rpm and increases to ~60.1% at 600 rpm. Convection from the ventilated channel becomes the dominant steady state heat transfer after ~160 rpm for the WBD disc whereas this only occurs after ~280 rpm for the pin-finned disc. The increased performance of the WBD disc when compared to that of the pin-finned disc is likely due to the larger surface of the ventilated channel (~44% larger than that of the pin-finned disc) as well as a heat transfer coefficient ~7% (at 50 rpm) to ~14% (at 600 rpm) larger than for that of the pin-finned channel.

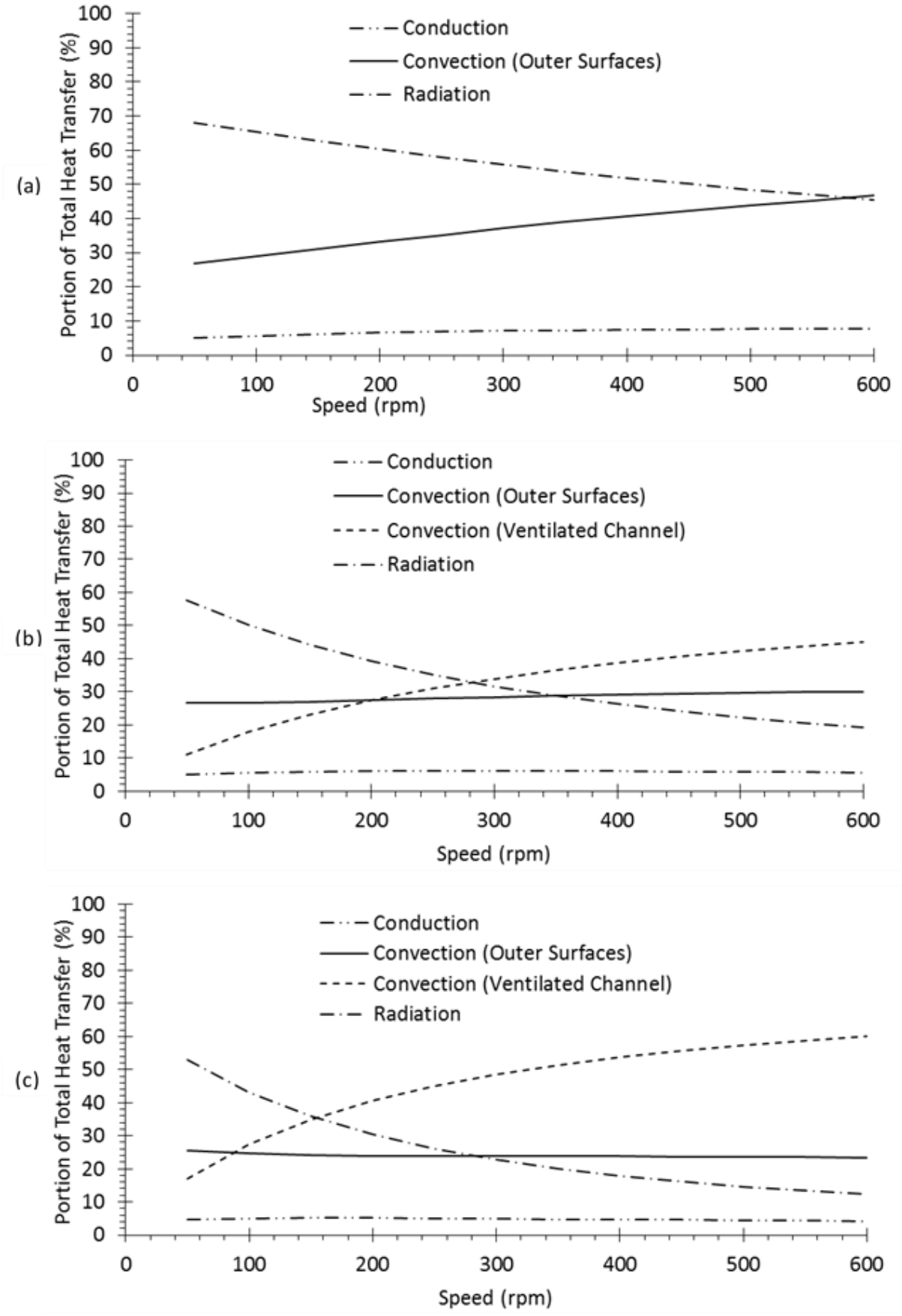


Figure 26: Steady state heat transfers as percentages of the total energy for the solid (a), pin-finned (b) and WBD (c) discs at a braking power of 2 kW.

5.6 Comparison of the Thermal Performance of Solid, Pin-Finned and WBD Discs in Representative Driving Scenarios

The temperature prediction model was used to simulate several representative driving scenarios, namely: (1) an emergency braking event manoeuvre, (2) an urban driving cycle and (3) drag braking.

5.6.1 Emergency braking

The predicted surface temperature during a 0.5 g braking event from 60-0 km/h, simulating an emergency stop of a medium sized truck (8000 kg with a tyre radius of ~0.5 m and 2 axles), is shown in Figure 27. The WBD disc reaches a peak temperature ~11 °C higher than the pin-finned or solid discs. The drop in surface temperature towards the end of the manoeuvre is due to the reduced braking power at lower speeds and the heat absorption to the inner material. The duration of an emergency braking event is too short for the improved heat transfer dissipation mechanism of the discs with ventilated channels to have an effect on the surface temperature. The surface temperature is chiefly influenced by the energy absorption and conductive ability of the brake disc material. Doubling the convective heat transfer from the outer surfaces of the solid brake disc results in the same temperature

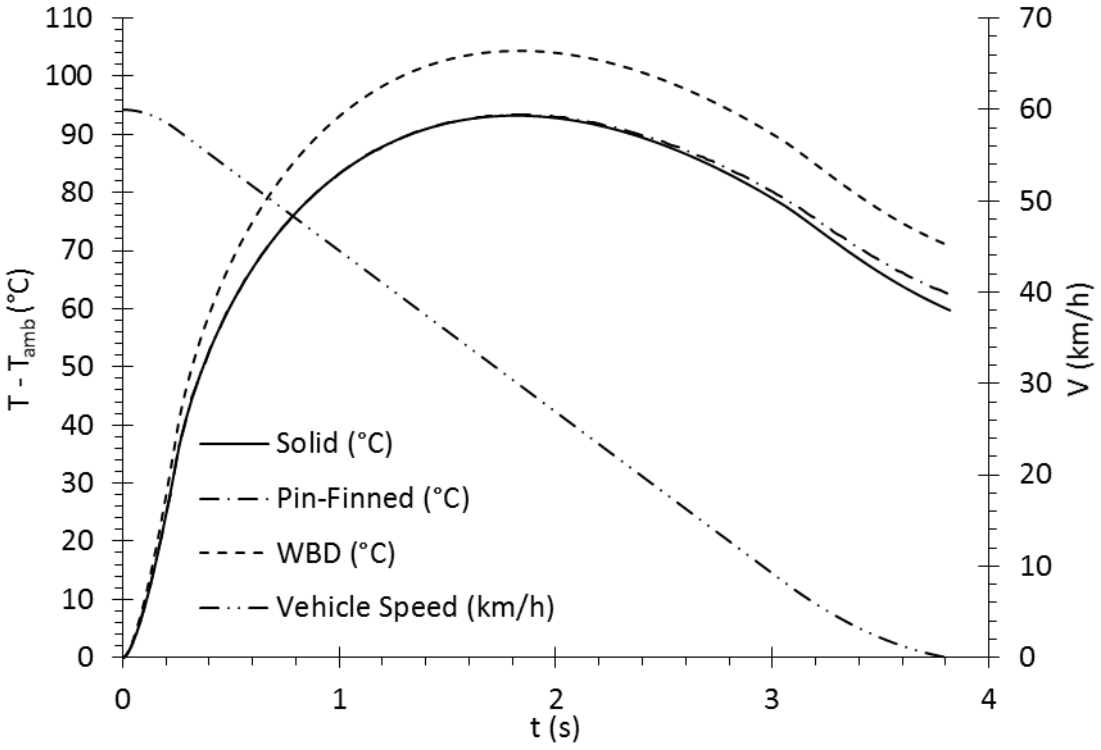


Figure 27: Temperature rise during a 0.5g braking event from 60 - 0 km/h.

response given in Figure 27. Table 6 shows that the peak temperature is dependent on material properties and is not effected much by any increase in convective heat transfer.

Table 6: Percent change in peak temperature for the corresponding property change of the solid disc during the emergency braking manoeuvre.

Property	Change in Property (%)	Change in Peak Temperature (%)
Density	+4%	-1.94
	-4%	2.06
Specific Heat	+4%	-1.44
	-4%	1.50
Convective Heat Transfer	+100%	-0.09
Thermal Conductivity	+2.5%	-1.24
	-2.5%	1.29

5.6.2 Urban driving

Using the temperature prediction model a representative urban driving cycle was simulated: a medium sized truck was braked from 80-20 km/h at a constant deceleration of 0.3 g, followed by an acceleration of roughly 0.03 g back to 80 km/h, after 120 s the braking cycle was re-initiated and the cycle was repeated 9 times and after the final acceleration the vehicle was maintained at 80 km/h until 1400 s had passed (Figure 28). The mass of the two axle truck was taken as 8000 kg.

The surface temperature rise is relatively constant for each brake application (~110 °C, ~112 °C and ~ 126 °C for the solid, pin-finned and WBD discs respectively).Table *7* indicates that the temperature rise is primarily governed by the material properties of the brake disc resulting in the solid disc displaying a lower increase in temperature. During the relatively short period of the brake application, the braking energy does not have sufficient time to be conducted to the inner surface of the ventilated channel. The solid disc (which can absorb more energy) outperforms the ventilated discs if only the short duration of a single brake application is considered. After 1400s, the solid disc temperature is ~255 °C, the pin-finned disc temperature is ~215 °C and the WBD disc temperature is ~170 °C. The extended time period allows the greater dissipative convective heat transfer mechanisms in the ventilated

discs to reduce the disc surface temperatures. Figure 29 shows the effect of increasing the convective cooling has on the surface temperature response, with a marked decrease during the acceleration phases with little difference made to the temperature increases under brake application. During transient braking (the temperature has not reached steady state) the temperature response is dependent on the material properties and specifically the effect these have on the energy absorption capabilities.

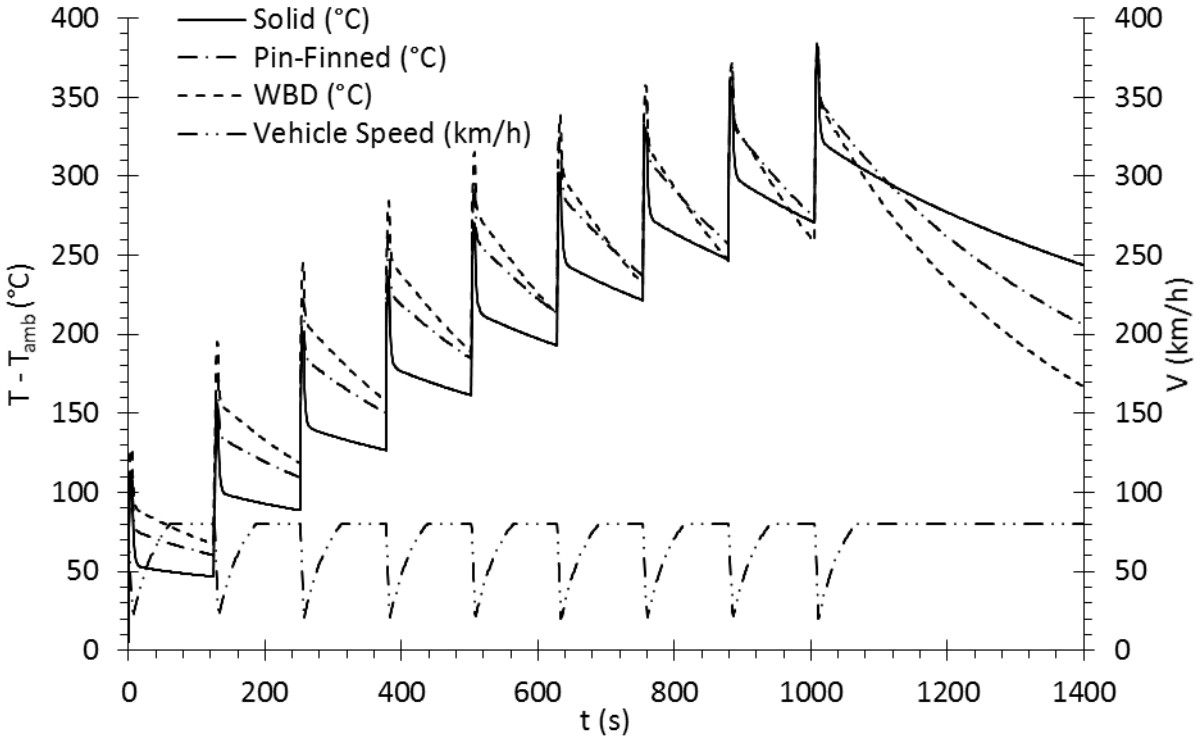


Figure 28: Simulated brake cycling from 80 - 20 km/h at a deceleration of 0.3g.

Table 7: Percent change in average temperature rise for the corresponding property change of the solid disc during the urban driving scenario.

Property	Change in Property (%)	Change in Average Temperature Increase (%)
Density	+4%	-1.91
	-4%	2.03
Specific Heat	+4%	-1.41
	-4%	1.48
Convective Heat Transfer	+100%	-0.17
Thermal Conductivity	+2.5%	-1.24
	-2.5%	1.29

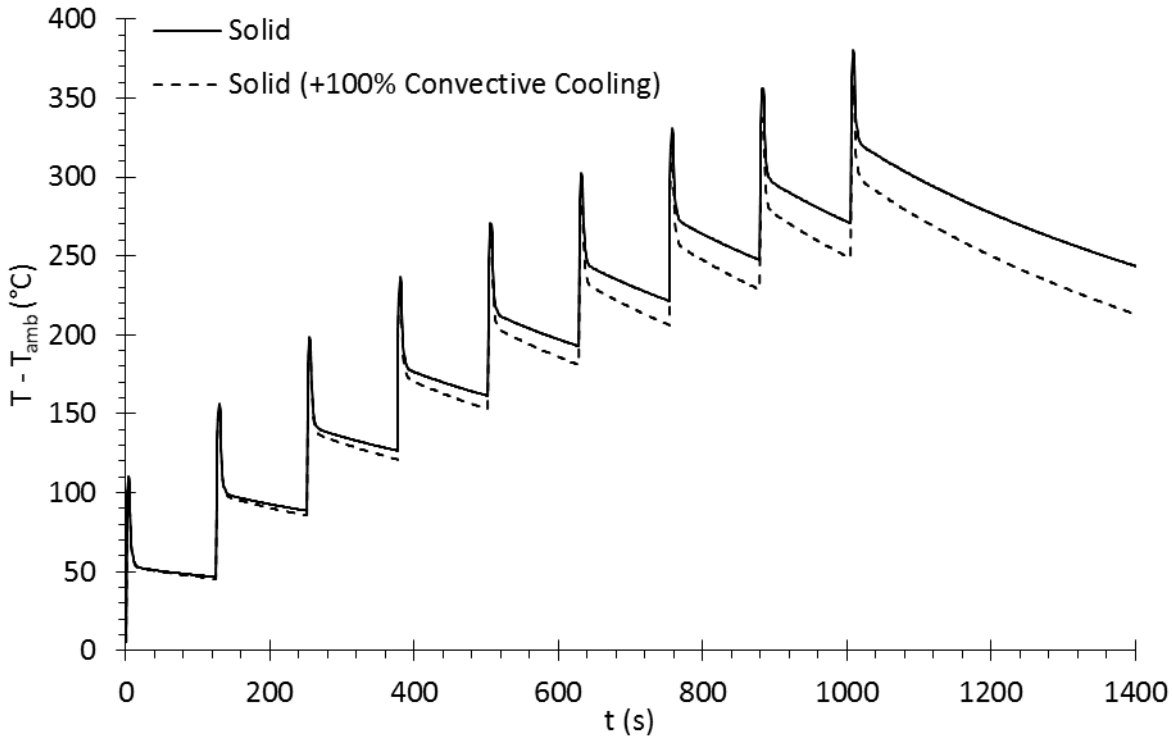


Figure 29: Urban braking scenario with +100% convective cooling for the solid disc.

5.6.3 Drag braking

The safe braking time (defined as the time taken for the average brake disc surface temperature to reach 600 °C under drag braking conditions) for various road gradients at 60 km/h (for a 2 axle vehicle of 8000 kg with a tyre radius of ~0.5 m) is shown in Figure 30 for the three types of brake discs tested. When the gradient is steeper than approximately 1.5% the required drag braking power is large enough (greater than ~8 kW) that the subsequent surface temperature rise is rapid enough that any convective advantage obtained from the ventilated discs is negated and the surface temperature response is chiefly dictated by the thermal capacity and related material properties of the disc. With gradients lower than ~1.5% the required drag braking power is low enough that subsequent surface temperature rise relative to the conduction through the material allows for the convection from the ventilated channel to contribute a more significant portion to the overall thermal performance.

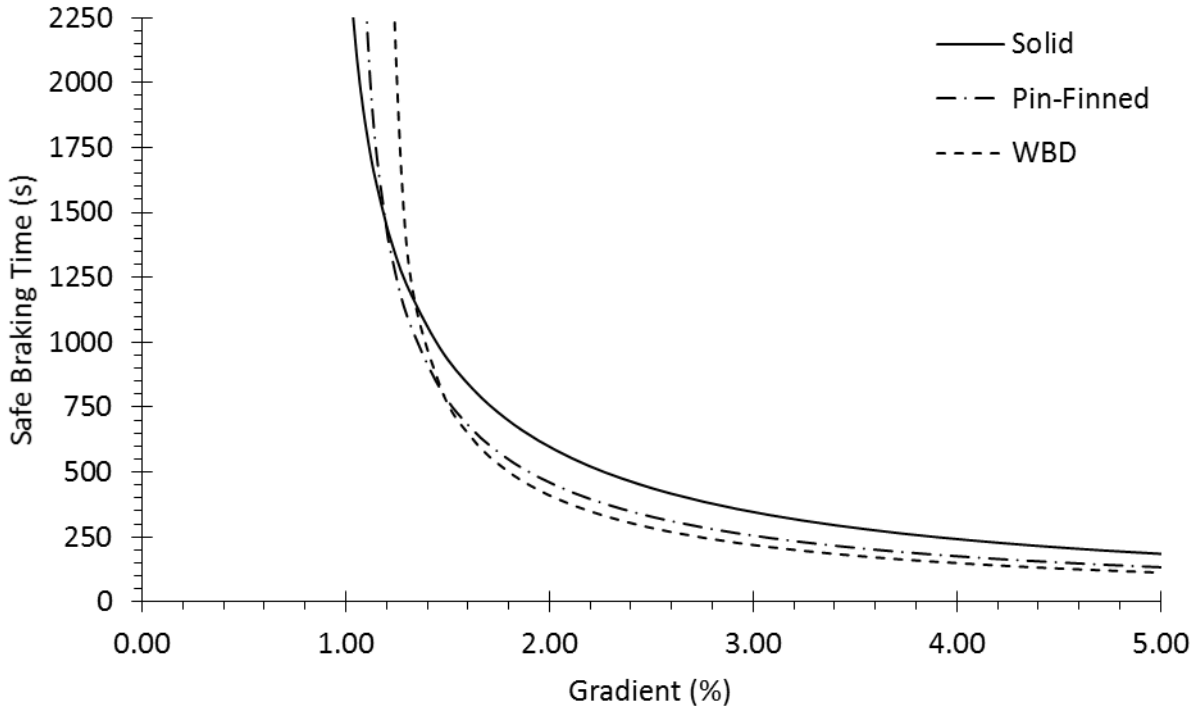


Figure 30: Safe drag braking times versus road gradient at 60 km/h.

6 CONCLUSIONS AND RECOMMENDATIONS

The operating temperature of a solid, pin-finned and WBD brake disc was experimentally measured at a braking power of 2 kW at speeds of 20 km/h, 30 km/h and 50 km/h (100 rpm, 150 rpm and 250 rpm respectively). Temperature prediction models for the solid, pin-finned and WBD discs were developed using the finite difference method in conjunction with heat transfer coefficients obtained from the literature. The models showed a steady state correlation to the experimental data of 0.46%-3.65% (1.6-13.1 °C). The conclusions drawn were as follows:

1. At t ≈ 1000 s for a constant braking power of 2 kW, the solid brake disc displayed surface temperatures lower than that for the pin-finned disc across the speeds tested and surface temperatures lower than for that of the WBD disc at the speeds of 100 rpm and 150 rpm (Figure 11). The WBD disc exhibited a decreased surface temperature at 250 rpm when compared to the solid and pin-finned discs. This due to the fact that at low speeds the heat transfer is dominated by the energy absorption up until ~580 rpm for the pin-finned disc and ~240 rpm for the WBD disc after which the convective heat transfer from the ventilated channel dominates (Figure 24).
2. At steady state for a constant braking power of 2kW, the solid and pin-finned discs exhibited similar steady state surface temperatures at 100 rpm after which the pin-finned disc exhibited lower surface temperatures when compared to the solid disc (Figure 12). The WBD disc exhibited lower steady state surface temperatures across all the speeds tested when compared to the solid and pin-finned discs. The convective cooling from the ventilated channel of the pin-finned disc becomes the dominant heat transfer mechanism only after ~280 rpm whereas for the WBD disc the convective cooling from ventilated channel becomes the dominant heat transfer mechanism after ~160 rpm (Figure 26).
3. During the emergency braking manoeuvre at 0.5 g from 60-0 km/h the surface temperature response of the disc is predominantly governed by the thermal capacity of the brake disc (and related material properties) rather than the dissipation of heat through radiation, convection or conduction; resulting in the solid and pin-finned discs outperforming the WBD disc (Figure 27 and Table 6).

4. During the simulated urban driving cycle (Figure 28) the surface temperature rise on each brake application is dependent mostly on the thermal capacity of the brake disc (and associated material properties) rather than the dissipation of the heat through radiation, convection or conduction (Table 7). Conversely, during the acceleration and cruising phases the surface temperature response is dominated by the dissipative mechanisms (Figure 29).
5. For a drag braking event at 60 km/h at gradients higher than ~1.5% (or a drag braking power greater than ~8 kW) the surface temperature response is chiefly governed by the thermal capacity (and the related material properties). For gradients less than ~1.5% the safe braking time increases with increasing the dissipation of heat through convection in the ventilated channel.

While the WBD has shown to potentially introduce significant thermal performance improvements several areas need to be investigated further before the WBD disc can be used in vehicles:

1. The torsional and compressive strengths of the WBD core need to be tested to determine if it can cope with typical braking loads and temperatures.
2. The WBD discs need to be used in the field in a trial comparison with conventional discs so as to determine their brake pad and disc life.
3. Possible contamination of ventilated brake discs, with specific focus on the WBD concerning the accumulation of brake dust or debris in the tightly packed core under normal operating conditions.

The current work has characterised the thermal response of various brake discs (solid, pin-finned and WBD) at varying speeds and in particular the portion of heat dissipated through the dissipative mechanisms of conduction, convection through the outer surfaces, convection through the ventilated channel, radiation and absorbed (stored) in the disc. Further work can be done to visulaise flow patterns within the ventilated cores to understand and further enhance the brake disc cooling.

7 REFERENCES

[1] A. J. Day and T. P. Newcomb, "The Dissipation of Frictional Energy from the Interface of an Annular Brake Disc," *Proc IMechE Part D: J Automobile Engineering,* vol. 198, pp. 201-209, 1984.

[2] R. Limpert, *Brake Design and Safety*, 3rd ed. Warrendale, USA: SAE International, 2011.

[3] A. Day, *Braking of Road Vehicles*: Oxford, 2014.

[4] R. G. Mortimer, L. Segel, H. Dugoff, J. D. Campbell, J. C.M, and R. W. Murphy, "Brake Force Requirement Study: Driver-Vehicle Braking Performance as a Function of Brake System Design Variables. Contract FH-11-6952," ed: Highway Safety Research Institute, 1970.

[5] M. Duzgun, "Investigation of Thermo-Structural Behaviors of Different Ventilation Applications on Brake Discs," *J Mech Sci Technol,* vol. 26, pp. 235-240, 2012.

[6] S. K. Rhee, M. G. Jacko, and P. H. S. Tsang, "The Role of Friction Film in Friction, Wear and Noise of Automotive Brakes," *Wear,* vol. 146, pp. 89–97, 1991.

[7] R. Limpert, "Cooling Analysis of Brake Disc Rotors," *SAE,* vol. 751014, 1975.

[8] R. Limpert, "The Thermal Performance of Automotive Disc Brakes," *SAE,* vol. 750873, 1975.

[9] L. M. Wallis, "A Comparison of Bi-Directional Disc Brake Rotor Passage Designs," 2003.

[10] D. C. Sheridan, J. A. Kutchey, and F. Samie, "Approaches to the Thermal Modeling of Disc Brakes," *SAE,* vol. 880256, 1988.

[11] T. Mew, T. Kim, K. J. Kang, and F. Kienhofer, "Transient Thermal Comparison of Solid and Ventilated Brake Discs," presented at the 9th South African Conference on Computational and Applied Mechanics, Somerset West, 2014.

[12] T. Mew, K. J. Kang, F. Kienhofer, and T. Kim, "Transient Thermal Response of a Highly Porous Ventilated Brake Disc," *Proc IMech Part D: J Automobile Engineering,* 2014.

[13] H. B. Yan, T. Mew, M. G. Lee, K. J. Kang, T. J. Lu, F. W. Kienhofer, and T. Kim, "Thermo-Fluidic Characteristics of a Porous Ventilated Brake Disc," MSc, Faculty of Engineering and the Built Environment, University of Witwatersrand, Johannesburg, 2014.

[14] H. B. Yan, T. Mew, M. G. Lee, K. J. Kang, T. J. Lu, F. W. Kienhofer, and T. Kim, "Thermofluidic Characteristics of a Porous Ventilated Brake Disk," *Journal of Heat Transfer,* vol. 137, 2015.

[15] K.-J. Kang, "Wire-Woven Cellular Metals: The Present and Future," *Progress in Materials Science,* vol. 69, pp. 213-307, 2015.

[16] F. Kienhofer, S. Zedi, K. J. Kang, and T. Kim, "Characterising the Thermal Performance of a Novel Lightweight Brake Disc with a Wire-Woven Ventilated Channel at Varying Speeds, EB2016-SVM-030," presented at the SAE EuroBrake Conference, Milan, Italy, 2016.

[17] R. Parker and T. Newcomb, "The Performance and Characteristics of the Disc Brake," 1964.

[18] P. Hwang, X. Wu, and Y. Jeon, "Repeated Brake Temperature Analysis of Ventilated Brake Disc on the Downhill Road," 2008.

[19] E. Palmer, R. Mishra, and J. D. Fieldhouse, "A Computational Fluid Dynamic Analysis on the Effect of Front Row Pin Geometry on the Aerothermodynamic Properties of a Pin-Vented Brake Disc," *Proc IMechE Part D: J Automobile Engineering,* vol. 222, pp. 1231-1245, 2008.

[20] F. P. Incropera, D. P. DeWitt, T. L. Bergman, and A. S. Lavine, *Fundamentals of Heat and Mass Transfer*, 7th ed. New York, USA: Wiley, 2011.

[21] L. Wallis, E. Leonardi, B. Milton, and P. Joseph, "Air Flow and Heat Transfer in Ventilated Disc Brake Rotors with Diamond and Tear-Drop Pillars," *Numerical Heat Transfer, Part A, Applications: An International Journal of Computation and Methodology,* 2001.

[22] H. Kasem, J. Thevenet, X. Boidin, M. Siroux, P. Dufrenoy, B. Desmet, and Y. Desplanques, "An Emissivity-Corrected Method for the Accurate Radiometric Measurement of Transient Surface Temperatures during Braking " *Tribology International,* vol. 43, pp. 1823-1830, 2010.

[23] P. D. Richardson and O. A. Saunders, "Studies of Flow and Heat Transfer Assocoiated with a Rotating Disc," *Mechanical Engineering Science,* vol. 5, pp. 336-342, 1963.

[24] F. Krieth, R. M. Manglik, and M. S. Bohn, *Principles of Heat Transfer*, 7th ed., 2011.